

A dynamical model for the shallow-to-deep transition of Amazonian moist atmospheric convection

Article

Published Version

Creative Commons: Attribution 4.0 (CC-BY)

Open Access

Vraciu, C. V. (2026) A dynamical model for the shallow-to-deep transition of Amazonian moist atmospheric convection. *Journal of Geophysical Research: Atmospheres*, 131 (5). e2025JD045128. ISSN 2169-8996s doi: 10.1029/2025JD045128 Available at <https://centaur.reading.ac.uk/129260/>

It is advisable to refer to the publisher's version if you intend to cite from the work. See [Guidance on citing](#).

To link to this article DOI: <http://dx.doi.org/10.1029/2025JD045128>

Publisher: American Geophysical Union

All outputs in CentAUR are protected by Intellectual Property Rights law, including copyright law. Copyright and IPR is retained by the creators or other copyright holders. Terms and conditions for use of this material are defined in the [End User Agreement](#).

www.reading.ac.uk/centaur

CentAUR

Central Archive at the University of Reading

Reading's research outputs online

A Dynamical Model for the Shallow-to-Deep Transition of Amazonian Moist Atmospheric Convection

Cristian V. Vraciu^{1,2} ¹Faculty of Physics, University of Bucharest, Bucharest–Măgurele, Romania, ²Department of Meteorology, University of Reading, Reading, UK**Key Points:**

- The shallow and deep convective clouds are modeled under a unified framework
- A dynamical model for the diurnal cycle of convection is developed and tested in Amazonian idealized cases
- The present conceptual model offers a promising step toward new unified cloud-convection prognostic models

Correspondence to:C. V. Vraciu,
c.vraciu@reading.ac.uk**Citation:**

Vraciu, C. V. (2026). A dynamical model for the shallow-to-deep transition of Amazonian moist atmospheric convection. *Journal of Geophysical Research: Atmospheres*, 131, e2025JD045128. <https://doi.org/10.1029/2025JD045128>

Received 11 AUG 2025

Accepted 14 FEB 2026

Abstract The development of deep convection and the timing of storm convection initiation over land are generally poorly represented by weather and climate models, probably due to the poor representation of the interaction between shallow and deep convection. The present work aims to present a prognostic model for the shallow-to-deep transition of Amazonian convection in which the shallow and deep clouds are described under a unified framework. Three types of clouds are considered in the present model: shallow cumuli, cumulus congestus, and deep cumulonimbus clouds. The model is based on the idea that the shallow-to-deep transition of atmospheric convection is primarily controlled by the interaction between updrafts and passive cloud volumes (non-convective cumulus cloud volumes in the decaying stage) from which moist air can be entrained in the updrafts. In this framework, the cold pools accelerate the shallow-to-deep transition due to a larger cloud-updraft interaction, allowing the updrafts to be less susceptible to entrainment of dry environmental air. A dynamical model for the diurnal cycle of shallow and deep is obtained and tested against idealized large-eddy simulations. For idealized cases of Amazonian atmospheric convection, it is shown that the model represents the transition from shallow to deep convection reasonably well, showing that the model could lead to improvements in the forecast for storm convection initiation.

Plain Language Summary Weather and climate models often struggle to accurately represent when and how storms begin to form over land. This is likely because they do not capture well the interaction between nonprecipitating clouds and deeper storm systems. The goal of this study is to introduce a new approach that treats the transition from shallow to deep convection as part of a dynamic system. The proposed model simulates the daily cycle of cloud development, from small, shallow clouds in the morning to deep storm clouds in the afternoon. It is built on the idea that the transition to deep convection is strongly influenced by how rising air currents (updrafts) interact with nearby cloud volumes, from which they can draw in moist air. In this framework, cold pools—cool air that spreads out near the surface after rain—play a key role by increasing this interaction and helping updrafts avoid dry air, which usually weakens them. The model is tested against idealized high-resolution numerical simulations and shows promising results in capturing this transition. This suggests the model could help improve forecasts of when storms are likely to develop.

1. Introduction

Predicting the diurnal cycle of shallow and deep convection is crucial for accurate weather forecasting and climate modeling, as it governs precipitation timing, intensity, and severe weather events. Additionally, it is essential for various economic sectors, including aviation, agriculture, and energy planning, as it directly impacts decision-making and operational efficiency. Multiple recent studies have explored the physical processes governing the diurnal cycle of shallow and deep Amazonian convection as well as the interaction between them (e.g., Böing et al., 2012; Grabowski, 2023; Khairoutdinov & Randall, 2006; Kurowski et al., 2018, 2024; Manco & Figueroa, 2025; Vraciu et al., 2023, 2025). However, weather and climate models continue to predict the onset of deep stormy clouds 2–5 hr earlier than observed or simulated by large-eddy simulations (LES) within a diurnal cycle (e.g., Couvreur et al., 2015; Harvey et al., 2022; Tao et al., 2023). This discrepancy arises because, within a diurnal cycle, convective parameterization schemes typically trigger deep convection as soon as Convective Inhibition (*CIN*) is negligible and Convective Available Potential Energy (*CAPE*) is large enough to support the development of cumulonimbus clouds (Guichard et al., 2004). In reality, even under these conditions, the transition often requires several hours to occur—a phenomenon referred to as “convective memory” (Colin et al., 2019; Colin & Sherwood, 2021; Daleu et al., 2020)—or it may not take place at all within a single diurnal cycle over land (e.g., Tian et al., 2021; Zhuang et al., 2017).

© 2026. The Author(s).

This is an open access article under the terms of the [Creative Commons Attribution License](https://creativecommons.org/licenses/by/4.0/), which permits use, distribution and reproduction in any medium, provided the original work is properly cited.

Most convective parameterization schemes used in weather prediction and climate models rely on the mass-flux approach. These formulations conceptualize a convective cloud as a single entraining plume that interacts exclusively with environmental air, represented by the mean resolved state (Arakawa & Schubert, 1974; De Rooy et al., 2013; Vraciu, 2024). Consequently, the convective mass flux in these schemes is calculated solely based on the large-scale state, ignoring cloud-cloud interactions and sub-grid heterogeneity within a given grid box. Because the convective mass flux evolves only in response to the slow changes in the large-scale state, these schemes struggle to capture the rapid transitions from shallow to deep convection observed during a diurnal cycle over land where the atmosphere is already unstable at the onset of shallow convection, without substantially changing during the shallow-to-deep transition (Bechtold et al., 2004; Couvreux et al., 2015; Song et al., 2024; Tao et al., 2023; Vraciu et al., 2025; Wu et al., 2009).

To predict the onset of deep, precipitating convection, some numerical models employ CIN-based triggering functions, which activate the deep convection scheme only when the kinetic energy of boundary layer updrafts exceeds the convective inhibition (e.g., Rio et al., 2009; Rio et al., 2013). However, this approach is still based on the fundamental structure of the parameterization scheme—it merely decides whether the scheme is switched on or off. Once triggered, the convective mass flux associated with deep convection typically transitions abruptly from zero to a fixed value corresponding to convective quasi-equilibrium, typically maintaining the quasi-equilibrium with the large-scale environment as long as the scheme remains active (Bechtold et al., 2014). A key limitation of this method is that it fails to represent the gradual development of deep convection from shallow convection, often leading to a premature onset of precipitation by several hours. To address this issue, some parameterization schemes have introduced additional constraints, such as requiring the presence of cold pools (CP) for deep cumulonimbus clouds to form, even when *CAPE* is already substantially large (e.g., Hohenegger & Bretherton, 2011; Suselj et al., 2019). Despite this improvement, the large *CAPE* at the triggering time still causes the convective scheme to produce precipitation immediately, without resolving the intermediate stages—from shallow non-precipitating cumuli to congestus and, eventually, deep cumulonimbus clouds. As a result, while these schemes may model the transition from congestus to cumulonimbus clouds, they do not fully correct the timing of precipitation onset. Moreover, as they heavily rely on the CP positive feedback in the shallow-to-deep transition, they are unable to represent the deepening of cumulus clouds from non-precipitating cumuli to congestus observed in simulations in which the CP are suppressed. Others proposed triggering functions based on a so-called dynamical *CAPE* (e.g., Cui et al., 2021; Xie et al., 2019), defined as the *CAPE* generation rate by large-scale advective forcing, in which deep convection is triggered only if the dynamical *CAPE* is positive.

The scope of this study is to obtain a dynamical system able to represent the evolution of shallow, congestus, and cumulonimbus cloud cover during the rapid transition from shallow to deep convection happening in a diurnal cycle over Amazonian land. The present model is based on the framework and conceptual picture of Vraciu et al. (2025), where a simple Lotka-Volterra model is proposed for the rapid shallow-to-deep transition. However, here we extend that study by incorporating the CP effect into the model in an explicit manner, and also by allowing the updraft velocity at the cloud base to follow a diurnal cycle. It should be noted that there are already a number of convection and cloud models based on the predator-prey framework. Nober and Graf (2005), for example, introduced a spectral convection model where cloud types compete for atmospheric instability using a Lotka-Volterra framework. Similar to the classical model by Arakawa and Schubert (1974), it relaxes the quasi-equilibrium assumption and allows for cloud-cloud interactions, though only indirectly via their influence on the mean atmospheric profile. Wagner and Graf (2010) expanded this approach by incorporating entrainment into cloud population dynamics, following Pan and Randall (1998), though this derivation has been debated by Plant and Yano (2011). Other models apply the predator-prey concept to different cloud regimes: for instance, Koren and Feingold (2011) and Feingold et al. (2015) modeled rain as a predator of stratocumulus clouds, mediated by aerosols and featuring explicit time delays, although not designed for deep convection. A predator-prey type model for shallow convection is also derived by Chen et al. (2025) to predict the evolution of the shallow cloud area distribution. Colin and Sherwood (2021) proposed a Lotka-Volterra model where convection and small-scale structures like CP and updrafts act as predators on large-scale atmospheric instability. Their approach introduces memory effects and resembles the discharge-recharge cycle in Yano and Plant (2012a), also connecting back to concepts from Nober and Graf (2005).

The paper is organized as follows. Section 2 presents the conceptual model and the derivation of the dynamical model. The CP feedback is introduced in Section 2.1. In Section 2.2, a simple parameterization for the updraft velocity is proposed, which is tested for an idealized case of Amazonian convection. In Section 2.3, the dynamical

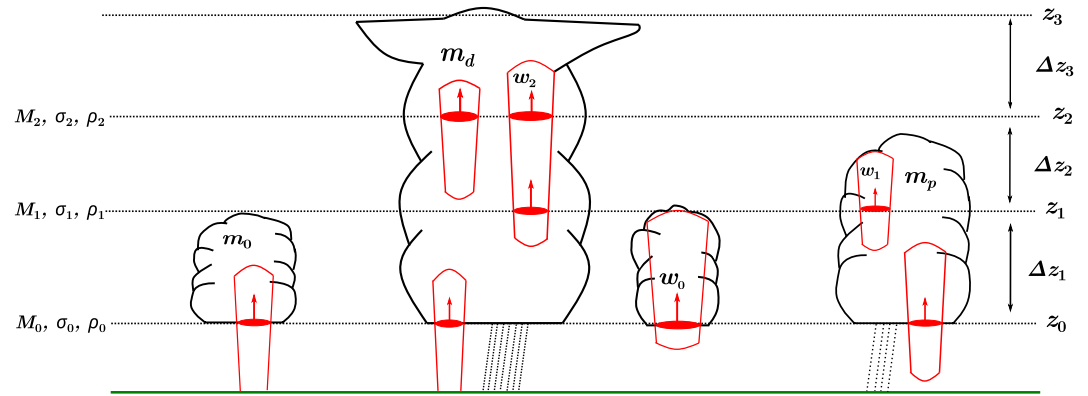


Figure 1. Schematics of the three-layer cumulus model. The clouds, denoted by the black contour, are represented from a lateral view, in which the updrafts are denoted by the red contour. The non-convective air within the clouds (i.e., not within the updrafts) represents passive cloud volumes.

model is derived, and its predator-prey dynamics are discussed. The model is tested in Section 3 against LES with and without suppressed CP and with constant surface fluxes (Section 3.1) and diurnal surface fluxes (Section 3.2). The predator-prey characteristics of the dynamical model in the diurnal cycle are tested in Section 3.3. The role of instability and relative humidity in the transition from shallow to deep convection in the dynamical model is analyzed in Section 4. In Section 5, the sensitivity of the model to the tuning parameters is analyzed. Conclusions and discussion are presented in Section 6.

2. Model Formulation

We consider that the cloud layer can be split into three layers with the depths Δz_1 , Δz_2 , and Δz_3 , as schematically illustrated in Figure 1. We thus consider three types of clouds: shallow cumuli, which are non-precipitating clouds, having a top at $z_1 = z_0 + \Delta z_1$, in which z_0 is the cloud base level; cumulus congestus, which are precipitating clouds and have a top at $z_2 = z_1 + \Delta z_2$; and deep cumulonimbus clouds (heavy precipitating clouds), with a cloud top at $z_3 = z_2 + \Delta z_3$. We denote by σ_0 the cloud area at cloud base, which is approximately the fractional area of all cloud species, by σ_1 the cloud cover at z_1 , which is approximately the fractional area of congestus and cumulonimbus clouds, and by σ_2 the cloud cover at z_2 , which we consider to be approximately the cumulonimbus clouds fractional area.

To obtain a dynamical model for the cloud cover of the three cloud species, we start from the budget equations for the air mass within the clouds in each layer:

$$\frac{dm_0}{dt} = M_0 - M_1 - \frac{m_0}{\tau_0}, \quad (1a)$$

$$\frac{dm_p}{dt} = M_1 - M_2 - \frac{m_p}{\tau_p}, \quad (1b)$$

$$\frac{dm_d}{dt} = M_2 - \frac{m_d}{\tau_d}, \quad (1c)$$

where m_0 is the air mass within the clouds (all types) in the first cloud layer, m_p is the air mass within the precipitating clouds (congestus and cumulonimbus) in the second cloud layer, m_d is the air mass within the deep cumulonimbus clouds in the third cloud layer, t is the time, M_j with $j = \overline{0, 2}$ represents the convective mass flux at level z_j , τ_0 is the lifetime of clouds in the first cloud layer, τ_p is the lifetime of precipitating clouds (congestus and cumulonimbus) in the second cloud layer, and τ_d is the lifetime of deep cumulonimbus clouds in the third cloud layer. A table of variables and constants is presented in Appendix A. Here, we assume that each cloud species decays following a simple decay rate. As is going to be seen, in the final system of equations for the cloud cover, the decay will take the form also assumed by Pan and Randall (1998) or Yano and Plant (2012b).

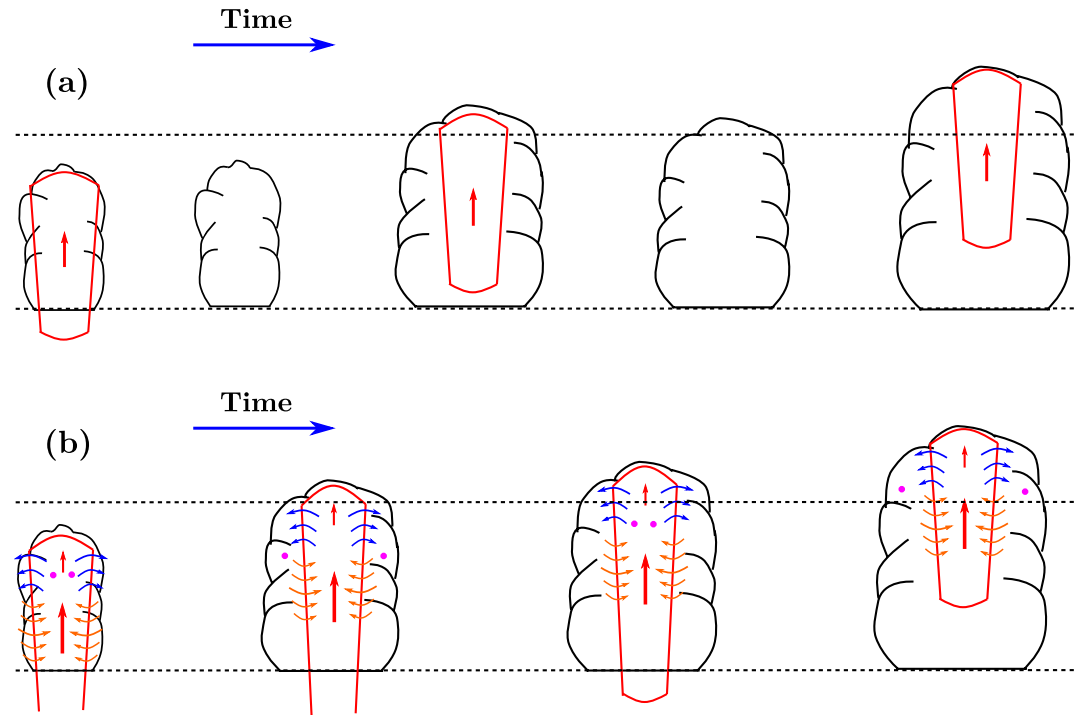


Figure 2. Schematics of the deepening of a cumulus cloud due to the cloud-updraft interaction. (a) Deepening due to the interaction of updrafts with preexisting clouds, formed by previous updrafts. (b) Deepening due to the re-entrainment of air of a single updraft with a large lifetime, as shown by the path of the two magenta particles. Here, the blue arrows denote detrainment of air from the updraft, creating passive cloud volumes, while the red arrows denote entrainment in the updraft. At the beginning, the updraft entrains dry air from the environment, losing its buoyancy rapidly, and detrains air close to the cloud top. After some time, the updraft will mostly entrain moist air from the passive cloud volumes, helping the updraft to better preserve its buoyancy and continuously deepening the cloud.

The mass flux at the cloud base (level z_0) is given by:

$$M_0 = \rho_0 \sigma_u w_0, \quad (2)$$

where ρ_0 , σ_u , and w_0 are the air density, updraft fractional area, and mean updraft velocity at the cloud base, respectively. Please note that throughout the paper, σ_u only refers to the updraft fractional area immediately below the cloud base, that is, at lifting condensation level (*LCL*) or at the top of the boundary layer. The mass flux at levels z_1 and z_2 are given by:

$$M_j = \rho_j \sigma_{int,j} w_j, \quad (3)$$

with $j = \overline{1,2}$, where ρ_j , $\sigma_{int,j}$, and w_j are the air density, interacting updraft fractional area, and mean updraft velocity at the level z_j , respectively. Here, by interacting with updrafts, we understand those updrafts that interact with passive cloud volumes, that is updrafts that entrain mostly the moist air within clouds (Figure 2). The interacting updraft fractional area is thus the fractional area of updrafts that entrain cloudy air. We thus consider here that the congestus clouds are formed if the updrafts reaching level z_1 entrain air from a shallow cumulus cloud. Similarly, a cumulonimbus cloud is formed if the updraft at level z_2 entrains air from a congestus cloud. By passive cloud volumes, we refer to non-convective cloudy air, and by updrafts, we refer to bulk air volumes that are rising. Thus, we consider that the updrafts can be defined based on a vertical velocity threshold criterion. We therefore consider that the updrafts can entrain non-saturated air from the environment or saturated air from the passive cloud volumes. We assume that there can be two possibilities for an updraft to entrain air from a passive cloud volume:

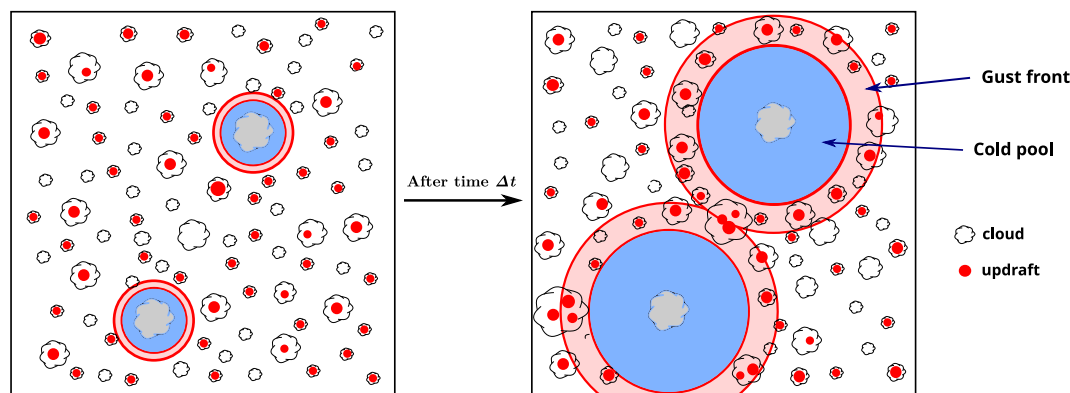


Figure 3. The effect of cold pools (CP) on cloud-updraft interaction. As the CP spread in the boundary layer in the time Δt , they inhibit convection in their areas, forcing the updrafts to develop near the gust fronts, forming clouds on a smaller area, thus facilitating the cloud-updraft interaction, resulting in wider and deeper clouds. The non-precipitating clouds are depicted here with white color while the precipitating clouds are depicted with gray color. The CP are represented by the blue color, and their gust fronts by a red contour. The convective updrafts are depicted by small red dots.

- if there are multiple updrafts developing in the same place in a period of time short enough such that the cloud created by the previous updraft has not completely decayed (Vraciu et al., 2023, 2025), as schematically represented in Figure 2a;
- if an updraft has a lifetime large enough such that, due to the toroidal motion of the updraft (Eytan et al., 2024; Hernández Pardo et al., 2025; Pinsky et al., 2023; Sherwood et al., 2013), the air detained by the updraft close to the cloud top is re-entrained by the updraft after some time, as schematically represented in Figure 2b.

2.1. Cold Pools Feedback

It has been shown by a relevant number of studies that the CP play an important role in the shallow-to-deep transition within a diurnal cycle (e.g., Böing et al., 2012; Kurowski et al., 2018; Schlemmer & Hohenegger, 2014; Vraciu et al., 2025). As also argued by Böing et al. (2012) and Vraciu et al. (2025), we consider here that the CP promote the deepening of moist convection because clouds generally form along gust fronts, with the deepest clouds developing at the intersections of these fronts (Böing et al., 2012; Fiévet et al., 2023; Fuglestedt & Haerter, 2020). This may be because clouds located at these junctions are surrounded by other clouds on all sides, reducing the entrainment of dry, non-cloudy air in their updrafts. As a result, the updrafts are able to gain more buoyancy, creating deeper clouds while also promoting wider cloud bases (Böing et al., 2012). A schematic of this effect is presented in Figure 3. It should be noted that the CP might also have a positive effect on the deepening of cumulus clouds because they might promote wider updrafts, which have smaller entrainment rates (Schlemmer & Hohenegger, 2014). However, recent studies show that the widening of updrafts during the shallow-to-deep transition is negligible compared to the widening of the cloud (Kurowski et al., 2024; Savre & Craig, 2023). The CP might also lead to longer-lasting updrafts along gust fronts (Fuglestedt & Haerter, 2020) promoting the re-entrainment effect schematically presented in Figure 2b.

Here, we present a parameterization for the interacting updraft fractional area $\sigma_{int,j}$ at level z_j that takes into account the CP feedback, for which a number of assumptions are made. First, we consider that the interacting fractional area is a sum of the interacting fractional area in the area not affected by the CP $\sigma_{int,j}^{(0)}$ and the interacting fractional area along the gust front $\sigma_{int,j}^{(gf)}$:

$$\sigma_{int,j} = \sigma_{int,j}^{(0)} + \sigma_{int,j}^{(gf)} \quad (4)$$

Second, we assume that $\sigma_{int,j}^{(0)}$ is given by the random overlap between the fractional area of passive cloud volumes at level z_{j-1} and the updraft fractional area at the top of the boundary layer σ_u . Assuming that the fractional area of passive cloud volumes at a given level is a fraction of cloud cover at that level, we get:

$$\sigma_{int,j}^{(0)} = \alpha_0 \sigma_{j-1} \sigma_u, \quad (5)$$

where α_0 is a proportionality coefficient related to the fraction of passive cloud volumes fractional area to the cloud cover. We thus consider that $\sigma_{int,j}^{(0)}$ is proportional to the updraft cloud cover at cloud base. We also consider here that $\sigma_{int,j}^{(0)}$ is proportional to the cloud cover at level z_{j-1} because for $\sigma_{j-1} = 0$ there cannot be interacting updrafts at level z_j , and for $\sigma_{j-1} = 1$ all updrafts reaching the level z_{j-1} develop within a cloud, so they are interacting. Note that we can also consider that $\sigma_{int,j}^{(0)}$ is proportional to σ_{j-1} at any positive power, but we consider here σ_{j-1} at the power 1 for simplicity. Because the CP are negatively buoyant (Tompkins, 2001; Torri et al., 2015), we also consider that within the CP, there are no updrafts able to reach the cloud level (Figure 3). Hence, we can write:

$$\sigma_u = \sigma_{u,0}(1 - \sigma_{cp}), \quad (6)$$

where $\sigma_{u,0}$ is the updraft fractional area at the top of the boundary layer in the absence of CP, and σ_{cp} is the CP fractional area.

Third, to obtain the fractional area of interaction updrafts along the gust fronts, we first consider that the fraction of updrafts σ_u can be written as a sum of fractional area of updrafts developing along gust fronts $\sigma_u^{(gf)}$ and fractional area of updrafts developing outside CP and gust fronts $\sigma_u^{(out)}$. After, we consider that $\sigma_u^{(out)} = (1 - \sigma_{gf})\sigma_u$, which leads to the following expression for the fractional area of updrafts developing along gust fronts: $\sigma_u^{(gf)} = \sigma_u \sigma_{gf}$, in which σ_{gf} is the gust fronts fractional area. The fraction of interacting updrafts at level z_j above the gust fronts is also given by the overlap between the updrafts and passive cloud volumes at level z_{j-1} , and thus, we have:

$$\sigma_{int,j}^{(gf)} \propto \sigma_{j-1} \sigma_{gf} \sigma_u. \quad (7)$$

Furthermore, we assume that the gust front fractional area is proportional to the CP fractional area. Thus, we consider the following relation:

$$\sigma_{int,j}^{(gf)} = \alpha_{gf} \sigma_{j-1} \sigma_{cp} \sigma_u, \quad (8)$$

where α_{gf} is a coefficient given by the product:

$$\alpha_{gf} = (\text{probability for cloud - updraft interaction along gust fronts}) \times (\text{ratio between gust fronts area and cold pools area}).$$

We consider that almost all updrafts along the gust fronts are to some degree protected from the entrainment of dry air by shallow clouds (Böing et al., 2012; Fuglestedt & Haerter, 2020), and thus, we expect that the probability for cloud-updraft interaction along gust fronts is much larger than α_0 . As we also consider that the gust fronts area is with an order of magnitude smaller than the CP area, we assume that the coefficient α_{gf} is with an order of magnitude larger than α_0 .

Therefore, we obtain:

$$\sigma_{int,j} = \gamma \sigma_{j-1} \sigma_{u,0}, \quad (9)$$

where the parameter γ is given by:

$$\gamma = \alpha_0 \left(1 + \frac{\alpha_{gf}}{\alpha_0} \sigma_{cp} \right) (1 - \sigma_{cp}). \quad (10)$$

2.2. Updraft Parameterization

The dynamical system of Equation 1 also requires a parameterization for the updraft velocity at each level. In order to obtain a final dynamical system that is not heavily nonlinear, we are interested in having an updraft parameterization as simple as possible. Of course, more sophisticated parameterizations can be tested later on, but for the beginning, we want to show that even with simple parameterizations we get a reasonably accurate dynamical system. For w_0 , we consider that once CIN is very small (below a certain threshold), it is proportional to the convective velocity scale, and thus, we consider:

$$w_0 = c_0 \left(\frac{g}{\theta_0} z_0 SHF \right)^{1/3}, \quad (11)$$

where c_0 is a parameter, g is the acceleration due to gravity, $\theta_0 = 300$ K is a constant reference potential temperature, and SHF is the sensible surface heat flux. Here, we consider the cloud base z_0 for the calculation of w_0 instead of the inversion height because in the shallow-to-deep transition within a diurnal cycle, the two are almost proportional, and their variation is too small to make w_0 vary too much.

For the updraft velocity at levels z_j , with $j = \overline{1, 2}$, we aim to choose a parameterization that respects the following criteria:

- it is simple enough such that a dynamical system can be obtained;
- depends on the atmospheric instability;
- considers the cloud-updraft interaction discussed above;
- considers the CP feedback.

To achieve this, we start with a bulk plume model for the updraft velocity, following a number of simplifications to obtain a simple model for the updraft velocity at level z_j . Thus, we can consider the following plume model (De Rooy et al., 2013; Vraciu, 2022):

$$\frac{dw_u^2}{dz} = 2B - \varepsilon w_u^2, \quad (12)$$

where $w_u(z)$ is the updraft vertical velocity, $B(z)$ is the updraft buoyancy, and ε is the fractional entrainment rate. We can also consider that the buoyancy can be written as $B = \hat{B} b_z$, in which \hat{B} is a buoyancy amplitude and b_z is a function of z . Thus, solving the plume model between the cloud base and level z_j , we obtain the updraft velocity at level z_j as:

$$w_j^2 = w_0^2 \exp\left(-\varepsilon \sum_{j'=1}^j \Delta z_{j'}\right) + 2b_j \hat{B} \exp\left(-\varepsilon \sum_{j'=1}^j \Delta z_{j'}\right), \quad (13)$$

where j' is an index, and b_j is an integral constant given by:

$$b_j = \int_0^{\sum_{j'=1}^j \Delta z_{j'}} e^{\varepsilon z'} b_z(z') dz', \quad (14)$$

where z' is a vertical coordinate. Typically, $\varepsilon \sim 2 \cdot 10^{-3} \text{ m}^{-1}$ (Jo et al., 2025; Romps, 2010; Xu et al., 2021), and we consider that $\sum_{j'=1}^j \Delta z_{j'} \geq 3 \cdot 10^3$ m, which means that the product $\varepsilon \sum_{j'=1}^j \Delta z_{j'}$ is much larger than 1, implying that we can neglect the first term in the right-hand side (RHS) of Equation 13, obtaining:

$$w_j = \left[2b_j \hat{B} \exp\left(-\varepsilon \sum_{j'=1}^j \Delta z_{j'}\right) \right]^{1/2}. \quad (15)$$

\hat{B} is a complicated function of $CAPE$, and for cloud-updraft interaction, we can also assume that \hat{B} is a function of cloud cover (Vraciu et al., 2023), and thus, we may consider that \hat{B} is also proportional to the fraction of updrafts that are interacting, as:

$$\hat{B} = \beta_0 \frac{CAPE}{EL - z_0} \frac{\sigma_{int,j}}{\sigma_{u,0}}, \quad (16)$$

where β_0 is a constant and EL is the equilibrium level (the level of neutral buoyancy for a non-entraining parcel). Thus, if all updrafts are interacting, then $\sigma_{int,j}/\sigma_{u,0} = 1$, and then all updrafts are protected from entrainment of dry environmental air; hence, buoyancy only scales with $CAPE$. On the other hand, if there are no interacting updrafts, then we consider that the buoyancy at level z_j should be zero. It should be noted that we do not consider that the updrafts reaching level z_j only entrain cloudy air, but rather that they have to entrain some amount of cloudy air in order to be able to reach level z_j (Figure 2). Therefore, in our model, the ratio $\sigma_{int,j}/\sigma_{u,0}$ is related to the amount of cloudy air entrained by the updrafts between the cloud base and level z_j . Substituting in Equation 15, and using also Equation 9, we get the following very simple model for the updraft velocity at level z_j :

$$w_j = c \sqrt{2CAPE \gamma \sigma_{j-1}} \Theta(EL - z_j), \quad (17)$$

where Θ is the Heaviside step function, and c is a parameter given by:

$$c = \left[\frac{b_j \beta_0}{EL - z_0} \exp\left(-\varepsilon \sum_{j'=1}^j \Delta z_{j'}\right) \right]^{1/2}, \quad (18)$$

which we assume to be a constant.

Hence, the updraft velocity at level z_j is nonzero only if $EL > z_j$. It should also be noted that instead of $CAPE$, perhaps a more realistic cloud work function would allow for a better model, but we consider here $CAPE$ for simplicity.

2.2.1. Test of Updraft Parameterization

To test the model, here we consider the results obtained from a high-resolution LES reported in Vraciu et al. (2025). The simulation was conducted using the MISU-MIT Cloud and Aerosol model (MIMICA) (Savre et al., 2014), as detailed in Savre and Craig (2023). The simulation represents an idealized version of the original Large-scale Biosphere-Atmosphere (LBA) case, which is an Amazonian shallow-to-deep transition case described by Grabowski et al. (2006), with initial conditions and forcings adapted from Böing et al. (2012). Relative humidity was held constant at 80% up to an altitude of 6,000 m, decreasing linearly to 15% at 17,500 m. Latent and sensible surface heat fluxes were maintained constant at 343 W m^{-2} and 161 W m^{-2} respectively, which corresponds to the diurnal averages of the time-dependent fluxes considered in Grabowski et al. (2006). The model domain spans 102.4 km horizontally in both directions, with an upper boundary at 14.25 km. The horizontal grid spacing is 100 m, while the vertical spacing is 25 m below 1.5 km and increases geometrically above, reaching about 400 m at the top. An additional simulation was conducted with CP suppressed. This was achieved using the approach outlined by Böing et al. (2012), in which the tendencies of potential temperature and water vapor mixing ratio below the cloud base were nudged toward their horizontally averaged values over a timescale of 10 min. The reader is referred to Savre (2023a, 2023b) and Vraciu et al. (2025) for more details on the methodology of the simulations.

In Figure 4, a comparison is presented between the modeled data for the updraft velocity at cloud base (around 1,000 m), $z_1 = 4000 \text{ m}$, and $z_2 = 8000 \text{ m}$, and the data from LES at the same height. The modeled data is obtained using Equation 17 with input data for cloud cover at cloud base and the cloud cover at z_1 taken from LES. The cloud cover at each level is computed as the fractional area of cells in which the condensed water mixing ratio exceeds a threshold of 10^{-3} g m^{-3} . The input data for the CP fractional area σ_{cp} is also taken from LES and defined as the fractional area in which the temperature in the first LES vertical level is 1 K smaller than the

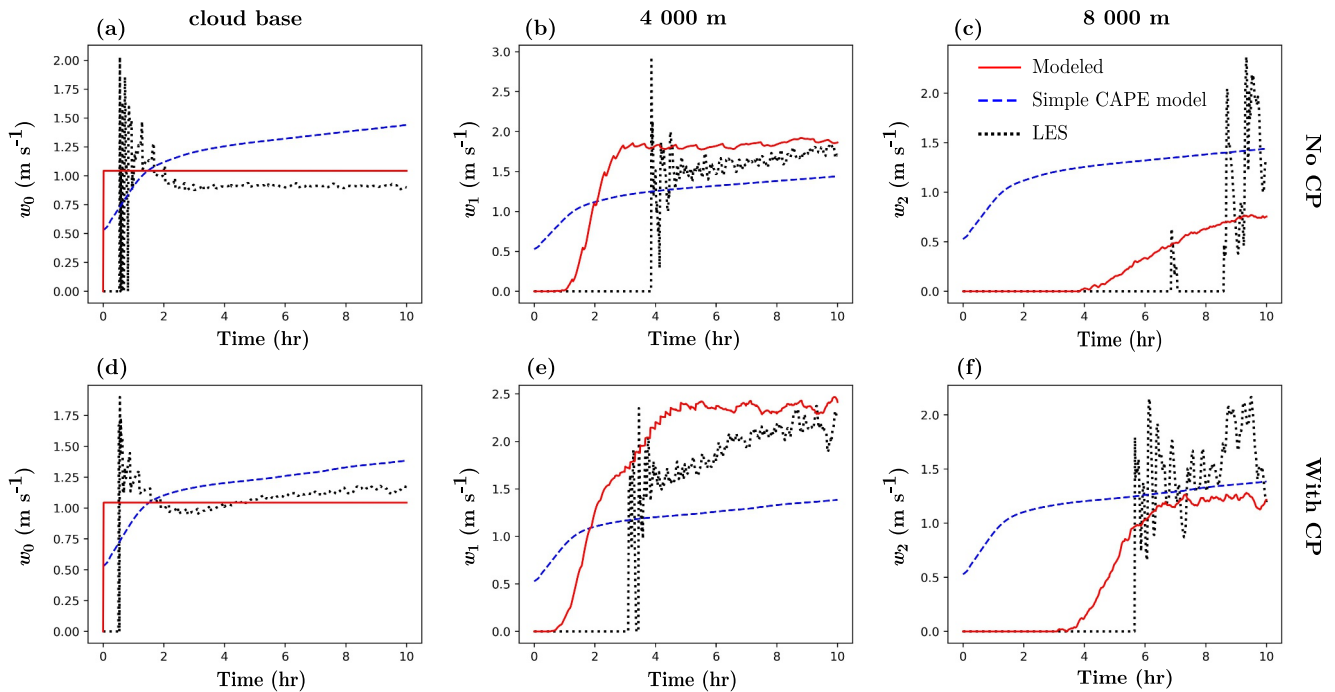


Figure 4. Updraft vertical velocity from the idealized large-eddy simulations (LES) at cloud base (a, d) 4,000 m (b, e) and 8,000 m (c, f). The data corresponding to the case with suppressed cold pools (CP) (No CP) are presented in the top panels (a–c), while the data with active CP are presented in the bottom panels (d–f). The data modeled with the parameterization model are plotted with red lines, for which the LES data for cloud cover, CP fractional area, and $CAPE$ have been used as input. The data for updraft velocity from LES are plotted with dotted black lines. In addition, a simple model proportional to $\sqrt{2CAPE}$ is plotted with dashed blue lines. For better visualization, LES data are smoothed with a third-order polynomial function.

average temperature at that level. The updraft velocity obtained from LES is computed at each level as the mean vertical velocity of the updraft cloudy cells, where the updraft cloudy cells are defined as the cloud cells in which the vertical velocity is above a threshold of 0.1 m s^{-1} . Here, we consider $c_0 = 6 \cdot 10^{-2}$, $c = 0.15$, $\alpha_0 = 0.25$, and $\alpha_{cp} = 3$. To show that a model that is only a simple function of $CAPE$ cannot work for the shallow-to-deep transition, we also test the following simple parameterization:

$$w_i = \chi \sqrt{2CAPE}, \quad (19)$$

where $\chi = 2 \cdot 10^{-2}$ is a constant. As shown by the blue lines in Figure 4, such a simple parameterization cannot accurately model the updraft velocity at each level.

To obtain a closed system of equations, the cold pool fractional area also requires parameterization. Here, for simplicity, we consider that it can be modeled as a linear function of congestus and cumulonimbus clouds cover, as:

$$\sigma_{cp} = \beta_1 (\sigma_1 - \sigma_2) + \beta_2 \sigma_2, \quad (20)$$

where $\beta_1 = 12$ and $\beta_2 = 15$ are coefficients, assumed here to be constants. The β_1 and β_2 coefficients might depend, however, on the environmental properties such as relative humidity or surface heat fluxes, which might have an impact on precipitation rate (Colin & Sherwood, 2021) and the spread of CP in the boundary layer (Fu & O'Neill, 2025). A sensitivity test to the β_1 and β_2 coefficients is presented in Section 5. The first and second terms in the RHS of Equation 20 represent the contribution of congestus and cumulonimbus clouds in the formation of CP, respectively.

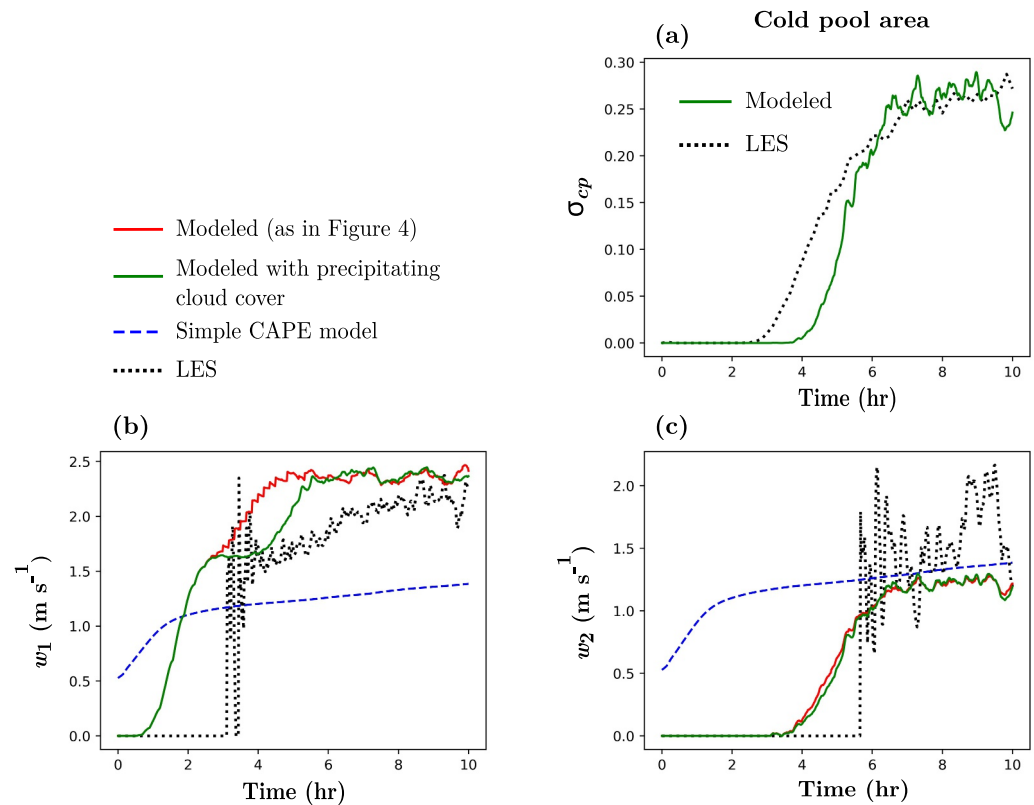


Figure 5. Cold pool fractional area parameterization. (a) The cold pool fractional area modeled with Equation 20 is compared with the fractional area obtained from large-eddy simulations as defined above. (b) Updraft velocity at level z_1 , modeled with Equation 17, in which the parameterization for the cold pool fractional area is used, is displayed with a green solid line. (c) As in (b) but at the level z_2 . The red solid line and the black dotted line are as in Figure 4.

In Figure 5a, the modeled CP fractional area using Equation 20 is plotted. As one may see, for this particular transition case, the model works reasonably. The updraft velocity at levels z_1 and z_2 modeled using Equations 17 and 20 is also plotted in Figure 5, showing good agreement with LES data.

An additional test is made against an idealized LES case with time-dependent surface fluxes reported in Kurowski et al. (2018). A total of four simulations are made in Kurowski et al. (2018): one pair of simulations with prescribed surface heat fluxes as in Grabowski et al. (2006) and one pair of simulations with interactive surface fluxes. Each pair of simulations has one case with active CP and one case with suppressed CP. All simulations are based on the LBA transition case with the initial profiles for temperature, moisture, and wind as in Grabowski et al. (2006). Here, we consider the data for the simulations with interactive surface fluxes, denoted as NOCP_i (for the case with suppressed CP) and CP_i (for the case with active CP) in Kurowski et al. (2018). The surface sensible heat flux (*SHF*) for the two simulations is presented in Figure 6. Please refer to Kurowski et al. (2018) for more details on the methodology of the simulations.

Data for updraft velocity at cloud base, 4,000 m, and 8,000 m altitude are extracted from Figure 15 of Kurowski et al. (2018) using an online data digitizer tool. The process of data collection could lead to some errors, but here we only use the data for testing our model, noting that these errors are negligible compared to the difference between our model and the LES data.

In Figure 7, modeled data for the updraft velocity using Equations 17 and 20 are compared with the LES data, showing reasonably good agreement. As before, LES data for cloud cover are used as input in our model. It should be noted that here the cloud cover is defined as the cloudy updraft fractional area as the two are assumed to be proportional and almost equal during the shallow-to-deep transition (Kurowski et al., 2018; Vraciu et al., 2025). These data are also extracted from Figure 15 of Kurowski et al. (2018) with the same method as for the updraft vertical velocity. Here, as *CAPE* does not vary substantially during the shallow-to-deep transition (e.g., Figure 4

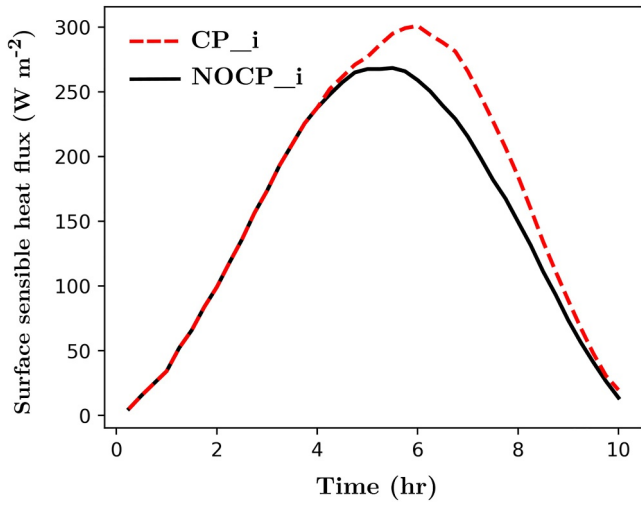


Figure 6. Surface sensible heat flux in the CP_i and NOCP_i simulation reported in Kurowski et al. (2018). The data are taken from Figure 6 of Kurowski et al. (2018) at 15 min interval.

of Efstathiou et al. (2024)), we use a constant value of $2,000 \text{ J kg}^{-1}$ to compute the updraft velocities at $z_1 = 4000 \text{ m}$ and $z_2 = 8000 \text{ m}$. Also, a constant value of $1,000 \text{ m}$ is considered for z_0 to calculate w_0 , which might have led to the difference between the modeled and LES data for w_0 in Figure 7. All parameters have the same value as before (Figures 4 and 5).

2.3. Dynamical Model for Cloud Cover

The aim of this study is to obtain a dynamical system describing the evolution of the three cloud species during the shallow-to-deep transition. Thus, we want to obtain a dynamical system for σ_0 , σ_1 , and σ_2 that is closed. To obtain this, we consider that all clouds have their tops at z_1 , z_2 , or z_3 , depending on their type. Hence, for the air masses within the clouds in the system of Equation 1 we can write:

$$m_0 = \bar{\rho}_0 \Delta z_1 \sigma_0, \quad (21a)$$

$$m_p = \bar{\rho}_1 \Delta z_2 \sigma_1, \quad (21b)$$

$$m_d = \bar{\rho}_2 \Delta z_3 \sigma_2, \quad (21c)$$

where $\bar{\rho}_0 = (\rho_0 + \rho_1)/2$, $\bar{\rho}_1 = (\rho_1 + \rho_2)/2$, and $\bar{\rho}_2 = (\rho_2 + \rho_3)/2$ are the mean air densities in the first, second, and third layer, respectively. Note that the masses are expressed per unit area and have units of kg m^{-2} .

Thus, putting all together, we obtain the following dynamical system for the cloud population of the three cloud species:

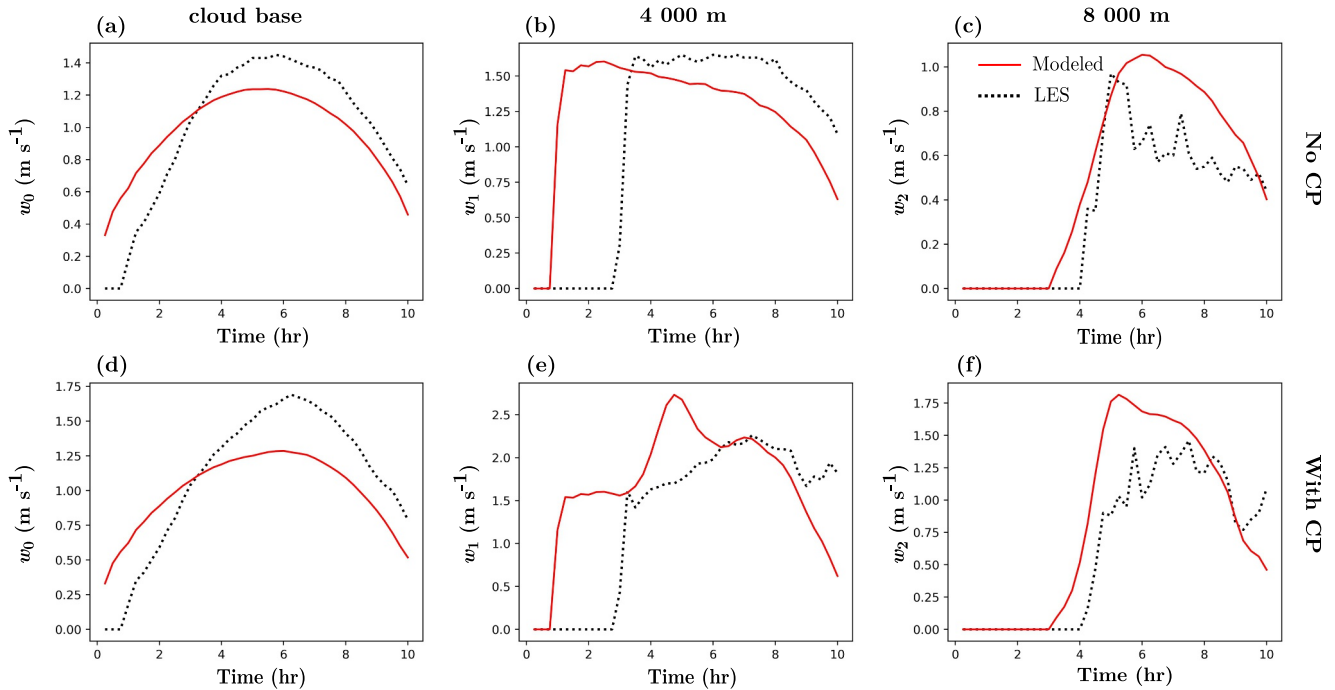


Figure 7. Updraft vertical velocity from the idealized large-eddy simulations (LES) reported in Kurowski et al. (2018) at cloud base (a, d) 4,000 m (b, e) and 8,000 m (c, f). The data corresponding to the case with suppressed cold pools (CP) (No CP) are presented in the top panels (a–c), while the data with active CP are presented in the bottom panels (d–f). The data modeled with the parameterization model are plotted with red lines, for which the LES data for cloud cover have been used as input. The data for updraft velocity from LES are plotted with dotted black lines. LES data for updraft velocity and cloud cover are taken from Figure 15 of Kurowski et al. (2018).

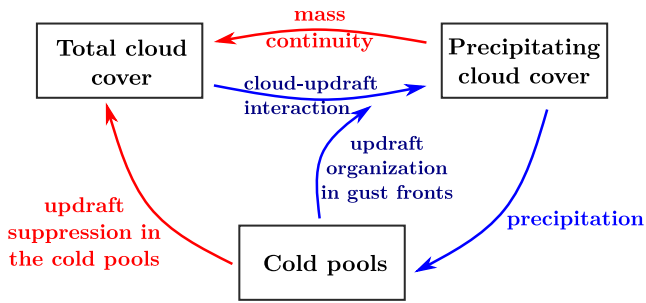


Figure 8. Schematics of feedback loops in the dynamical model. The blue arrow denotes a positive causality, while the red one denotes a negative causality. After Figure 13 of Vraciu et al. (2025).

$$\frac{d\sigma_0}{dt} = a_0 w_0 (1 - \sigma_{cp}) \sigma_{u,0} - b_0 w_1 \gamma \sigma_{u,0} \sigma_0 - \frac{\sigma_0}{\tau_c}, \quad (22a)$$

$$\frac{d\sigma_1}{dt} = a_1 w_1 \gamma \sigma_{u,0} \sigma_0 - b_1 w_2 \gamma \sigma_{u,0} \sigma_1 - \frac{\sigma_1}{\tau_p}, \quad (22b)$$

$$\frac{d\sigma_2}{dt} = a_2 w_2 \gamma \sigma_{u,0} \sigma_1 - \frac{\sigma_2}{\tau_d}, \quad (22c)$$

where $a_0 = \rho_0 / (\bar{\rho}_0 \Delta z_1)$, $b_0 = \rho_1 / (\bar{\rho}_0 \Delta z_1)$, $a_1 = \rho_1 / (\bar{\rho}_1 \Delta z_2)$, $b_1 = \rho_2 / (\bar{\rho}_1 \Delta z_2)$, and $a_2 = \rho_2 / (\bar{\rho}_2 \Delta z_3)$ are system constants.

The final step to close the system of equations is to consider a parameterization for $\sigma_{u,0}$. We consider, for simplicity, that in the absence of CP, the convective mass flux at the top of the boundary layer is proportional to the surface sensible heat flux. As the convective mass flux at the top of the boundary layer is proportional to the product of w_0 and $\sigma_{u,0}$, and since we consider that $w_0 \propto SHF^{1/3}$ (Equation 11), for $\sigma_{u,0}$ we consider the following very simple parameterization:

$$\sigma_{u,0} = \kappa SHF^{2/3} \Theta(SHF), \quad (23)$$

where κ is a constant.

The feedback loops in the dynamical model are summarized in Figure 8. The larger the total cloud cover (the cloud cover at cloud base), the larger the probability for cloud-updraft interaction, leading to an increase in the precipitating cloud cover (first term in the RHS of Equation 22b), which, in turn, leads due mass conservation to a reduction in the cloud cover at cloud base (second term in the RHS of Equation 22a). Precipitating clouds produce CP due to the precipitation evaporation in the boundary layer, forcing convection to form along the gust front, organizing convection, and increasing the cloud-updraft interaction (the first term in the RHS of Equation 22b increases due to a larger γ factor). Cold pools, however, also suppress convection, leading to a reduction of the total cloud cover (first term in the RHS of Equation 22a). As in Vraciu et al. (2025), we obtain a predator-prey type of dynamical system with the same feedback loops. However, here we consider the CP feedback explicitly, as opposed to Vraciu et al. (2025), where the feedback is only discussed qualitatively. We also consider a different parameterization for the updraft velocity, obtaining thus a different dynamical system, although both describe a predator-prey type of interaction between the cloud species. A parametric sensitivity study of the dynamical model is presented in Section 5.

3. Test of the Model

The model is tested against the idealized LES discussed above. First, we test the model against the shallow-to-deep transition case reported in Vraciu et al. (2025) in which constant surface fluxes are assumed, and then, we test the model against the data reported in Kurowski et al. (2018) in which the surface fluxes are time-dependent, mimicking a diurnal cycle.

3.1. Constant Surface Fluxes

The model is tested against the two simulations reported in Vraciu et al. (2025). As mentioned earlier, the simulations follow the LBA shallow-to-deep transition case (Grabowski et al., 2006), but with constant surface fluxes and with the initial horizontal wind set to zero. Two simulations are considered, both with the same set-up and initial conditions, but one with active CP and one with suppressed CP.

The modeled cloud cover data for the shallow-to-deep transition are plotted in Figure 9 with solid lines, together with the LES data from Vraciu et al. (2025), which are plotted with dotted lines. Although far from being a perfect match between the two data series, the model predicts the transition to deep convection reasonably well. Most notably, the model is able to capture two important features of the shallow-to-deep transition: (a) a reduction of

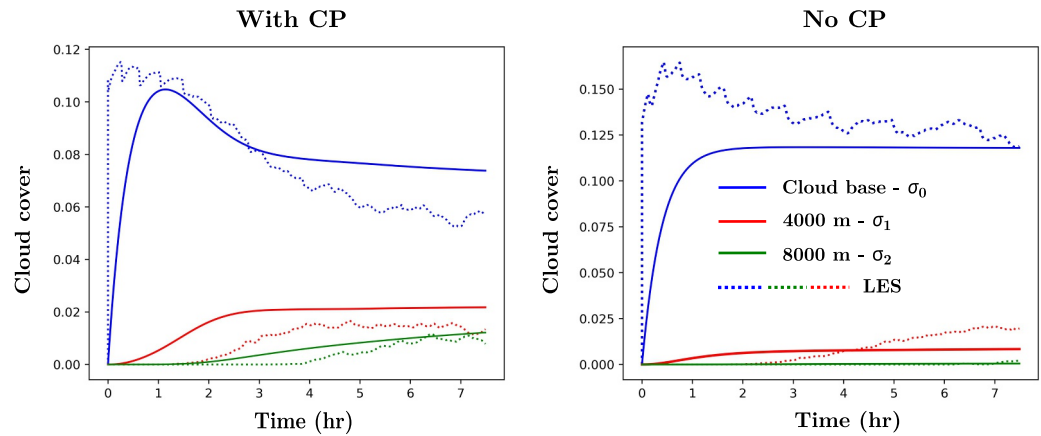


Figure 9. Time series of cloud cover at cloud base (blue lines), 4,000 m (red lines), and 8,000 m (green lines) during the shallow-to-deep transition case reported in Vraciu et al. (2025) for the case with active cold pools (CP) (left) and the case with suppressed CP (right). The solid lines represent data modeled with the present model, while the large-eddy simulations (LES) data is represented with dotted lines. Here, the LES data represent cloudy updraft fractional area, which is almost equal to cloud cover (see Figure A1 of Vraciu et al. (2025)).

cloud cover fractional area at cloud base in the presence of CP, and (b) a much smaller number of cumulonimbus clouds forming in the absence of CP. The data modeled with the dynamical model are obtained by solving the system of Equation 22 with the implicit Euler method with the following coefficients: $\kappa = 6.75 \cdot 10^{-3} \text{ m}^{4/3} \text{ W}^{-2/3}$, $\rho_0 = 1.1 \text{ kg m}^{-3}$, $\rho_1 = 0.787 \text{ kg m}^{-3}$, $\rho_2 = 0.516 \text{ kg m}^{-3}$, $\rho_3 = 0.324 \text{ kg m}^{-3}$, $\tau_0 = 25 \text{ min}$, $\tau_p = 1 \text{ hr}$, and $\tau_d = 3 \text{ hr}$. The values of the rest of the coefficients are as mentioned in Section 2.2.1.

3.2. Diurnal Surface Fluxes

The model is also tested against the two simulations reported in Kurowski et al. (2018) discussed in Section 2.2.1. As mentioned earlier, the simulations also follow the LBA shallow-to-deep transition case (Grabowski et al., 2006), but with interactive time-dependent surface fluxes (Figure 6).

The time series of modeled cloud cover and LES cloud cover (defined as cloudy updraft fractional area in Kurowski et al. (2018)) are plotted in Figure 10. The modeled cloud cover fractional areas are computed by solving the system of Equation 22 with the same values for the parameters as in the case with constant surface

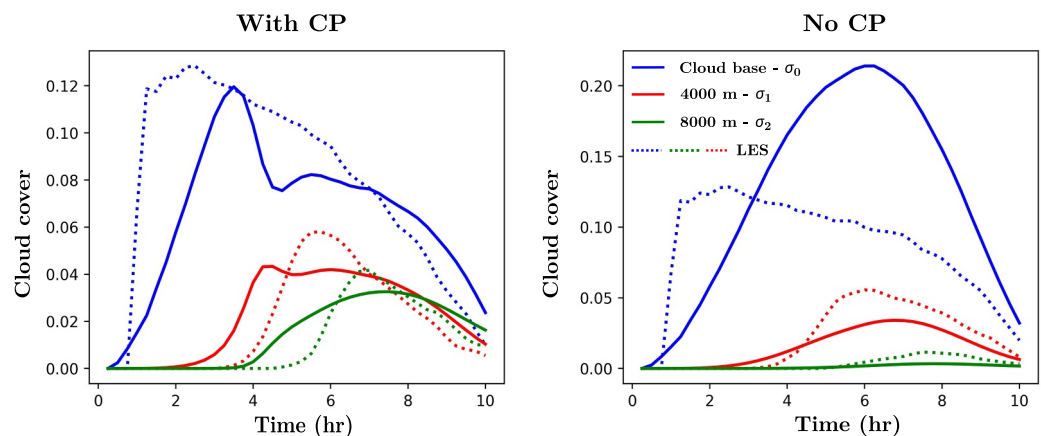


Figure 10. As in Figure 9 but for the transition case reported in Kurowski et al. (2018). The large-eddy simulations data has been extracted from Figure 15 of Kurowski et al. (2018) and represents the cloudy updraft fractional area.

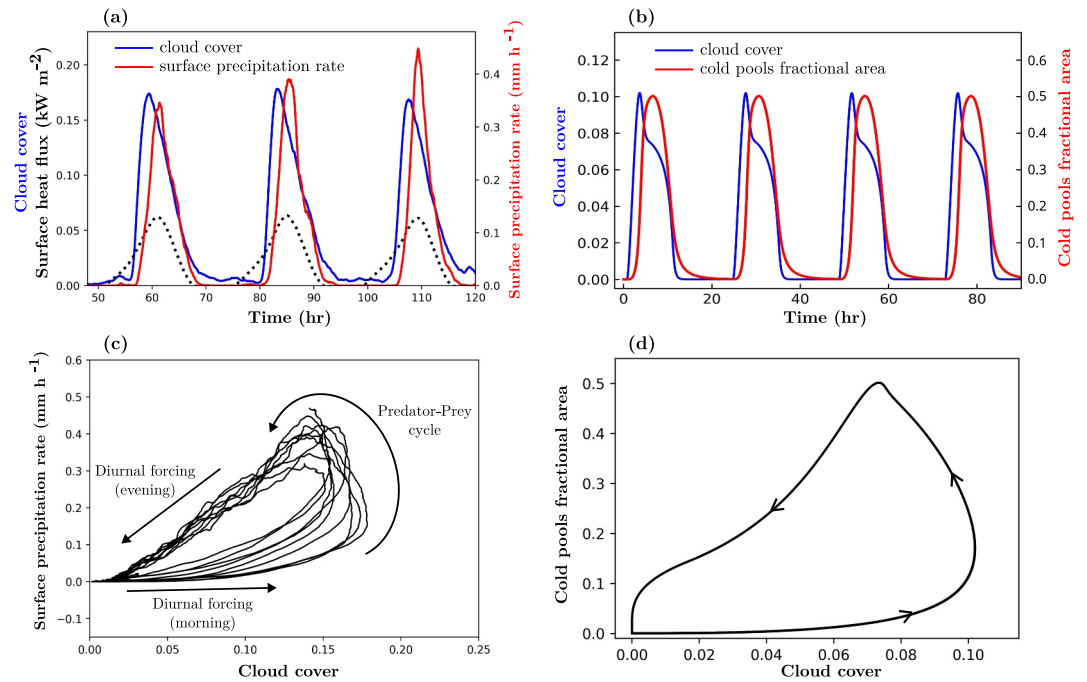


Figure 11. Cloud-precipitation system in a complete diurnal cycle of deep convection. (a) Time series showing cloud cover (blue solid line) and surface precipitation rate (red solid line) across three complete diurnal cycles. Surface heat flux is also included for reference (black dotted line). (b) Time series showing cloud cover (blue solid line) and cold pools fractional area (red solid line) across four complete diurnal cycles obtained with the present dynamical model. (c) Limit cycle representation of the cloud-precipitation system over the full 10-day simulation period, excluding the initial 2 days, which are treated as spin-up time. Data plotted in (a) and (c) are from Jensen et al. (2022), and the plots are adapted after Figure 14 of Vraciu et al. (2025). (d) Phase space of cloud cover—cold pools fractional area obtained for the data plotted in (b).

fluxes (Section 3.1). Although the model seems to give a consistent error for the cloud cover at cloud base in the case with suppressed CP, it predicts reasonably well the cloud cover in the case with active CP. It should be noted that the errors could also be due to a poor choice of the parameterizations for w_0 and $\sigma_{u,0}$. However, better alternatives for these two parameterizations can be considered without changing the dynamical model. Nevertheless, even with these very simple parameterizations, the model performs reasonably well for the cases with active CP.

3.3. Cloud-Precipitation System in the Diurnal Cycle

In this section, we test whether the model exhibits predator-prey characteristics in the cloud-precipitation system in a complete diurnal cycle, as shown by Vraciu et al. (2025) using LES data obtained by Jensen et al. (2022). In Figure 11a, the time series for the cloud cover and surface precipitation rate are plotted for a few days. The data are obtained by Jensen et al. (2022) and are openly available at Haerter (2021). The reader is referred to Jensen et al. (2022) for case description and methodological details. The phase space of the cloud-precipitation system modeled by Jensen et al. (2022) is represented in Figure 11c. For comparison, the data obtained with the present model are plotted in Figures 11b and 11d. The data modeled with our dynamical model are obtained by considering a diurnal cycle of the surface sensible heat flux given by:

$$SHF = 300 \left[\sin \left(\frac{2\pi t}{24 \text{ hr}} \right) - 0.2 \right] \text{ W m}^{-2}. \quad (24)$$

The rest of the setting is exactly as described in Section 3.2. Here, we plot the CP fractional area instead of the precipitation rate because in the dynamical model, a parameterization for the precipitation rate is not considered, but we assume that the precipitation rate is almost proportional to the cold pool fractional area, which is parameterized here with Equation 20.

As one may see, the dynamical model gives similar characteristics for the cloud-precipitation system as in the large-eddy simulation, but the match between the two is not perfect. Although there are some differences between the two sets of data, the model still predicts reasonably well predator-prey characteristics within a complete diurnal cycle of deep convection, especially considering the large number of approximations considered here and the simplicity of the model.

4. Role of Instability and Relative Humidity in the Shallow-to-Deep Transition

Both numerical and observational studies (e.g., Tian et al., 2021; Tian & Zhang, 2025; Varble et al., 2024; Viscardi et al., 2025; Wu et al., 2009) show that the atmospheric instability characterized by *CAPE* and the tropospheric environmental relative humidity are important factors for the shallow-to-deep transition within a diurnal cycle over land. Although a large value of *CAPE* is important for deep convection initiation, *CAPE* alone is often not a good predictor of deep convection onset (Jo et al., 2025; Miller et al., 2025; Tian et al., 2021). On the other hand, if *CAPE* is not too small, the tropospheric relative humidity plays a very important role in the transition from shallow to deep convection (Chakraborty et al., 2018; Jo et al., 2025; Tian et al., 2021; Viscardi et al., 2025; Wu et al., 2009), with larger relative humidity leading to a more rapid development of deep clouds.

The role of instability and environmental relative humidity in the deep convection initiation can be theoretically explained by a steady-state plume model (e.g., Morrison, 2017; Morrison et al., 2022). However, such a model cannot explain the gradual convective deepening during the rapid shallow-to-deep transition, during which the instability and humidity remain quite steady. Wu et al. (2009) shows that both *CAPE* and *RH* control the time-scale of shallow-to-deep transition, a time-scale which cannot be modeled with a steady-state plume model. Here, we study the role of instability and humidity in the present dynamical model. The relative humidity is introduced into the model by considering the cloud's lifetime depends on *RH* as follows:

$$\tau_r = \frac{\tau_{r,0}}{1 - RH}, \quad (25)$$

with $r \in \{0, p, d\}$, where $\tau_{0,0} = 6$ min, $\tau_{p,0} = 9$ min, and $\tau_{d,0} = 36$ min are constants. The role of relative humidity is introduced, thus by its influence on the cloud's lifetime. Larger *RH* means longer lifetimes, which means that the updrafts have more chances to interact with a shallow cloud, forming a deeper one. Note that this is different from the role of relative humidity in the dynamics of a plume model, where *RH* plays a role due to the evaporation-induced cooling within the moist plume due to the entrainment of dry environmental air (Morrison et al., 2022). However, the evaporation-induced cooling due to entrainment can also be considered in the present dynamical model by changing *CAPE* in Equation 17 with an entrainment-*CAPE* that considers the environmental relative humidity, such as the one derived, for example, by Peters et al. (2023). However, such a development is left for future work.

The cloud cover is plotted in Figure 12 for a diurnal cycle with the setting described in Section 3.3 for different values of *CAPE* and environmental relative humidity. Our model predicts that if the relative humidity is high, deep cumulonimbus clouds can develop even for relatively small values of *CAPE*, whereas in a dry atmosphere (small *RH*), cumulonimbus clouds develop only in a very small proportion, even when the instability is very large. Thus, our model qualitatively agrees with the observational and numerical studies. A quantitative test is left for a future study, in which the cloud-environment interaction will also be introduced in the dynamical model. To better appreciate the role of instability and relative humidity in the shallow-to-deep transition predicted by our model, in Figure 13, the dependence on *RH* of the maximum cumulonimbus cloud cover—defined as the maximum value of the cloud cover at z_2 —and of time t_* —defined as the time required for cumulonimbus clouds to reach a fraction of 10^{-5} —are represented, showing indeed a qualitative agreement with the observational and LES studies.

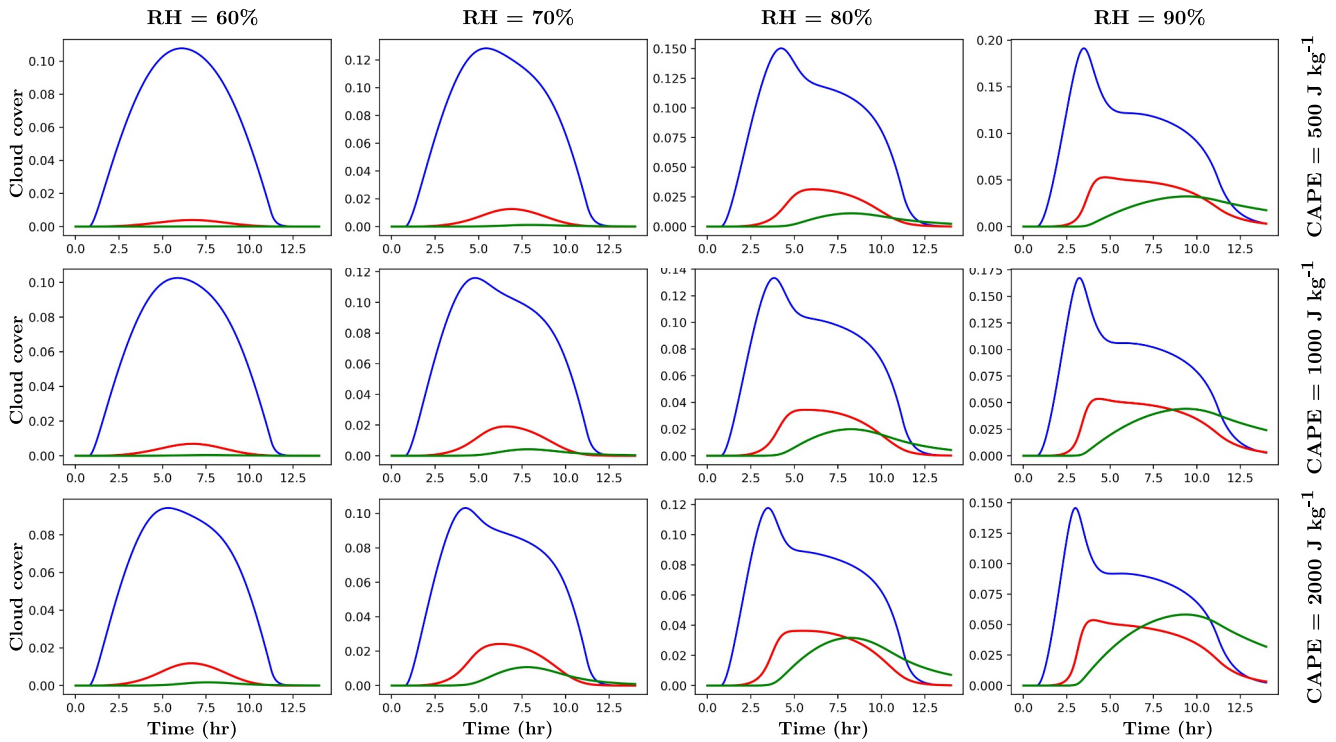


Figure 12. Dependence of cloud cover during a diurnal cycle on instability and environmental relative humidity for a $CAPE$ of 500 J kg^{-1} (top), $1,000 \text{ J kg}^{-1}$ (middle), and $2,000 \text{ J kg}^{-1}$ (bottom), and for four values of RH , as indicated on the plots. Cloud covers at cloud base are plotted with solid blue lines, cloud covers at z_1 are plotted with solid red lines, and the cloud covers at z_2 are plotted with green solid lines.

5. Parameter Sensitivity

To show the dependence of the system on the parameters that require tuning, a parametric study is carried out in the space of $\tau_{0,0}$, α_0 , α_{cp} , and c , limits of which are shown on the axes in Figure 14. Here, in order to reduce the number of parameters analyzed, we consider that $\tau_{p,0} = 1.5 \tau_{0,0}$ and $\tau_{d,0} = 6 \tau_{0,0}$. The parameters are varied two-by-two, while the other two take the default values considered in the previous sections ($\tau_{0,0} = 6 \text{ min}$, $\alpha_0 = 0.25$, $\alpha_{cp} = 3$, and $c = 0.15$). Each parameter is varied 30 times, resulting in a total of 5,400 different configurations, for which two metrics are evaluated: the time t_* and the maximum cumulonimbus cloud cover, which are defined in Section 4. The dynamical model is solved here with the setup used in Section 4, but with a constant $CAPE$ of $2,000 \text{ J kg}^{-1}$ and a constant RH of 80%.

The resulting contour maps are presented in Figure 14. As one may see, even for a large range of parameters, the system is quite stable, meaning that no extreme values for t_* or maximum cumulonimbus cloud cover are observed. Moreover, close to the default parameters, the differences in t_* are only about 1 hr, and those in maximum cumulonimbus cloud cover are about 0.02. The results show that although the solutions display a somewhat important sensitivity to $\tau_{0,0}$, they are not very sensitive close to the default value of 6 min. On the other hand, the solutions are quite sensitive to α_0 and α_{cp} , which control the interaction strength between clouds and updrafts. Sensitivity to the parameter c , related to the fraction of $CAPE$ converted into convective kinetic energy, also seems important, as expected.

An additional sensitivity test is made in the (β_1, β_2) -space (see Equation 20), where β_1 takes values between 2.5 and 17, and β_2 takes values between 5.5 and 20. The default values used for testing in Section 2.2.1 and Section 3 are $\beta_1 = 12$ and $\beta_2 = 15$. The resulting contour maps are shown in Figure 15, in which the results for which $\beta_1 > \beta_2$ are excluded because they are considered unphysical. It is shown that in this range, the time t_* is not very sensitive to the parameters, whereas the maximum cumulonimbus cloud cover is very sensitive. It is shown that

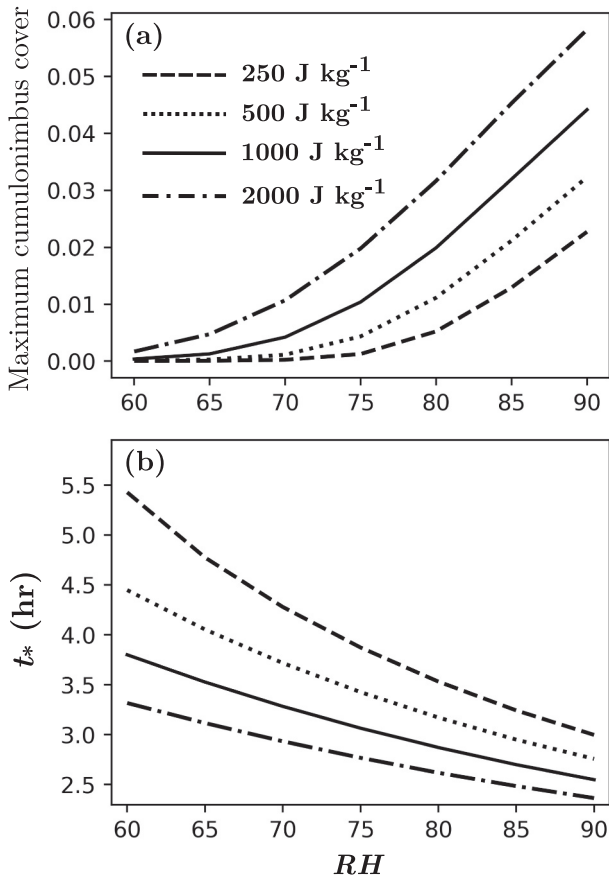


Figure 13. Dependence of maximum cumulonimbus cloud cover (a) and time t_* (b) on $CAPE$ and RH obtained with the dynamical model. Four values for $CAPE$ are considered here: 250 J kg^{-1} (dashed lines), 500 J kg^{-1} (dotted lines), $1,000 \text{ J kg}^{-1}$ (solid lines), and $2,000 \text{ J kg}^{-1}$ (dash-dotted lines).

shallow-to-deep transition by influencing cloud lifetimes and the likelihood of cloud–updraft interactions, in agreement with empirical findings.

Despite its strengths, the model remains idealized and includes several simplifications. The CP fractional area is parameterized rather than resolved explicitly, and updraft velocities are computed using basic functions of $CAPE$ and surface heat flux, which may not accurately capture the complex dynamics of real atmospheric updrafts. Although these simplifications are required here in order to obtain a dynamical system for the cloud cover, future improvements could include the development of a time-dependent plume model that considers both cloud–updraft interaction and CP feedback, in addition to the cloud–environment interaction, to be coupled to the dynamical system. Nevertheless, because of its simplicity and modular design, the model might be well-suited for integration into larger-scale weather prediction models, particularly within mass-flux-based convective parameterization schemes that use triggering functions. The model will allow the weather prediction models to capture a progressive deepening of the cumulus clouds instead of an instant switch from shallow to deep convective regimes. This can be done by replacing the mass–flux predicted by the deep convection scheme M_d with an adjusted mass–flux M'_d , as follows:

$$M'_d = \frac{\sigma_2}{\sigma_d} M_d, \quad (26)$$

for small values of the parameters, the maximum cumulonimbus cloud cover increases as the parameters increase, due to the positive feedback loop associated with CP. On the other hand, for large values of the parameters, the modeled CP fractional area is so large that it creates a negative feedback loop due to the convective suppression, and thus, it is observed from Figure 15b that larger values of the parameters lead to smaller values of the maximum cumulonimbus cloud cover.

6. Conclusions and Discussion

This study introduces a dynamical model that captures the evolution of shallow, congestus, and deep convective clouds within a unified framework, aimed at describing the rapid transition from shallow to deep convection during the diurnal cycle over land. Building on the conceptual understanding of cloud–updraft interactions, the model explicitly incorporates the role of CP, which are known to significantly influence the timing and organization of convective development.

The model performs well when tested against idealized LES, successfully reproducing the primary stages of cloud development: the formation of shallow cumuli, the emergence of congestus clouds, and the eventual deepening into cumulonimbus clouds. It accurately reflects the differences in convective evolution between simulations with active and suppressed CP, reinforcing the importance of cold pool dynamics in the transition process. The inclusion of cold pool feedback captures both their suppressive effect on convection within their area and their organizing influence along gust fronts, where cloud–updraft interactions are enhanced. This dual role allows the model to reproduce a realistic convective deepening pathway, consistent with previous observational and numerical studies.

The model also exhibits a predator–prey-like feedback in the cloud–precipitation system, replicating the cyclic behavior seen in LES studies. Furthermore, the model qualitatively confirms that while a high $CAPE$ is necessary, it is not sufficient to trigger deep convection on its own. In the present model, the environmental relative humidity plays a critical role in the

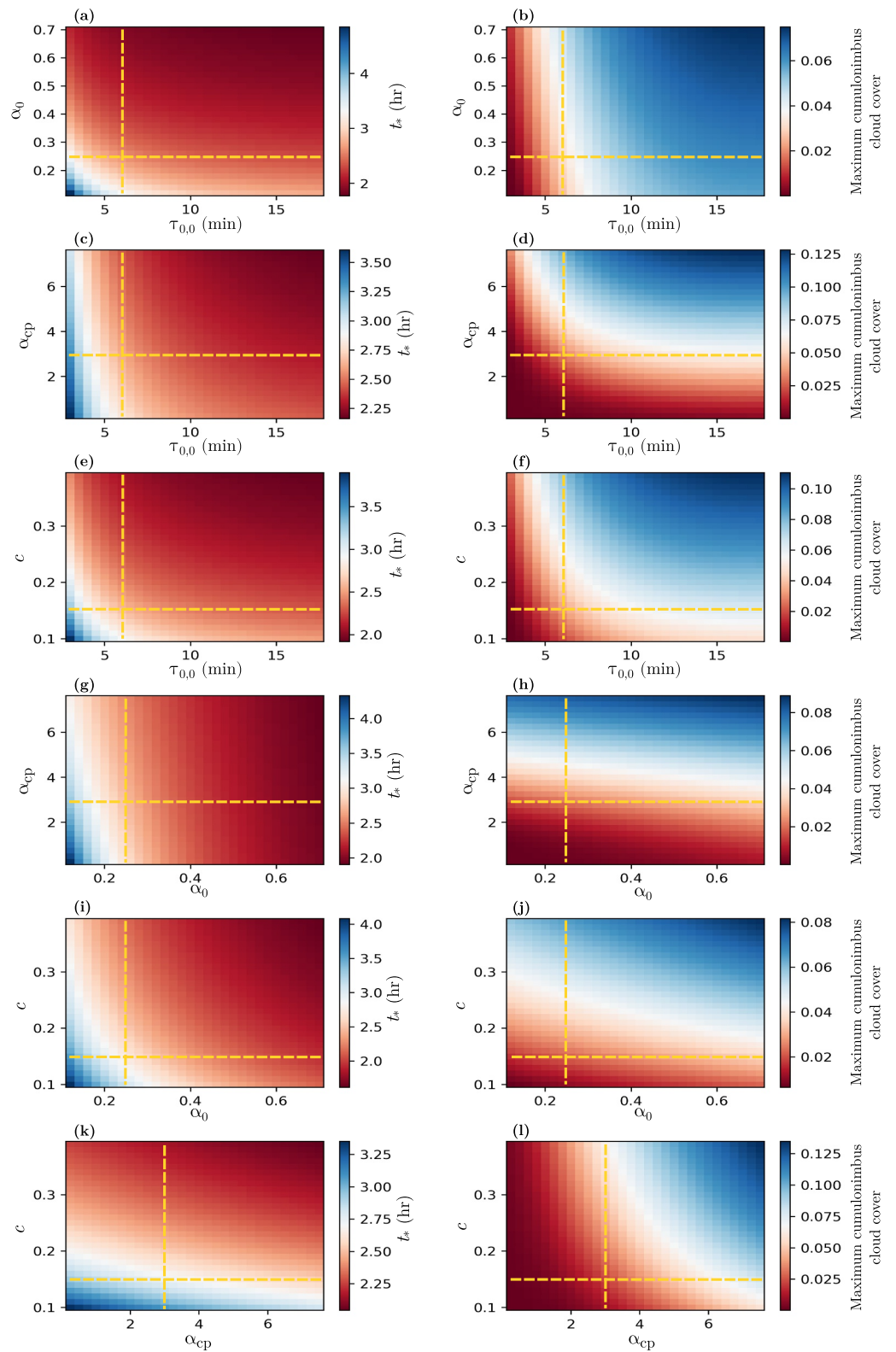


Figure 14. Evaluating the parameter space of the dynamical model. Left column (a, c, e, g, i, and k) shows the time t_* as a function of the parameter space, while the right column (b, d, f, h, j, and l) shows the maximum cumulonimbus cloud cover. Yellow dashed lines indicate the default values of the parameters used for testing.

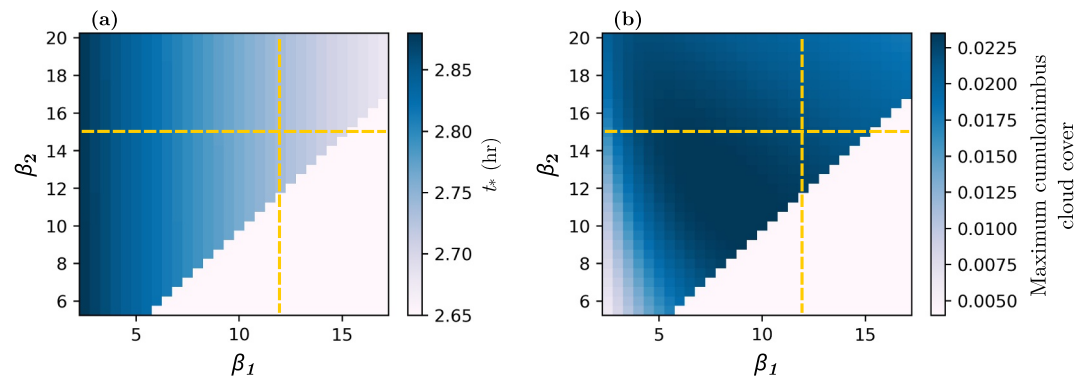


Figure 15. Sensitivity of time t_* (a), and maximum cumulonimbus cloud cover (b) in the (β_1, β_2) -space. Yellow dashed lines indicate the default values of the parameters.

where σ_2 is the fraction of cumulonimbus clouds modeled by the present dynamical model, and σ_d is the constant fractional area assumed by the deep convection schemes. The dynamical model can run in parallel to the cumulus parameterization scheme, starting to run only when there are conditions for deep convection initiation (e.g., large CAPE), and being shut down after deep convection reaches equilibrium, or after several hours. The model could, thus, be coupled to existing diagnostic convection schemes without altering their internal structure. This is because a diagnostic scheme may fail to capture the gradual shallow-to-deep transition but can correctly represent the convective mass flux once the system reaches quasi-equilibrium. Thus, the present dynamical model can modulate the amplitude of the convective mass flux during the shallow-to-deep transition without altering the existing diagnostic parameterization, but by only correcting the deep convection mass flux amplitude (Equation 26). While such an implementation is beyond the scope of the present study, outlining this pathway may guide future efforts to improve the timing and realism of convective onset in operational weather and climate models. However, here we only model the shallow-to-deep transition for Amazonian convection, and thus, it is not clear if the assumed values of the coefficients are universal or if they might need to take different values for different shallow-to-deep transition cases. Future research is thus needed to test whether the model can be implemented in a global model.

The present framework may also provide guidance for developing future data-driven or hybrid machine learning (ML) convective parameterizations. The dynamical model highlights a small set of physically interpretable variables that regulate the shallow-to-deep transition, such as CAPE, environmental relative humidity, or surface heat fluxes. Importantly, many of these quantities are already available as prognostic or diagnostic fields in numerical weather prediction systems and can be used as input in ML-based parameterizations. In addition, the present dynamical model itself provides a natural target for ML-assisted calibration. Because the model contains a relatively small number of physically interpretable parameters controlling cloud lifetimes, cloud-updraft interaction strength, and cold pool feedback, ML or Bayesian inference techniques could be used to estimate optimal parameter values from LES or observational data sets. Such an approach would allow the parameters to be trained in a regime-dependent manner, for example, as functions of environmental humidity, surface fluxes, or large-scale forcing, while preserving the underlying physical structure of the model.

In conclusion, the proposed dynamical model offers a promising step toward a more accurate representation of the shallow-to-deep convective transition. Its ability to capture essential features of the diurnal Amazonian convective cycle, including the influence of CP and environmental conditions, highlights its potential as a foundation for future parameterization schemes in atmospheric models. The proposed framework on which the dynamical model is built, and the difference to the current mass-flux view, is schematically presented in Figure 16. With continued refinement, it could contribute significantly to improving the timing and structure of convection in both weather forecasting and climate prediction frameworks.

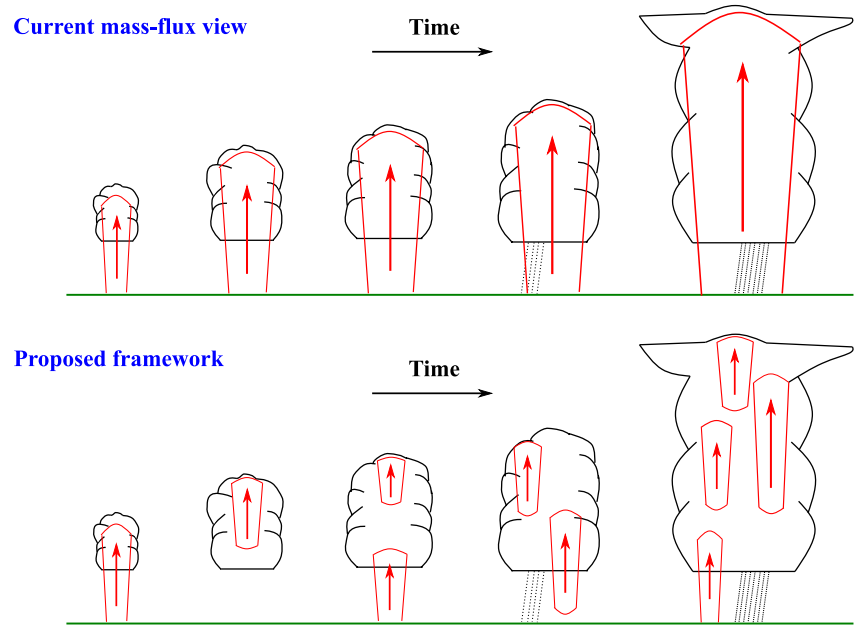


Figure 16. Deepening in the current mass-flux view (top) and the deepening in the present framework (bottom). In the current mass-flux parameterization, the deepening happens due to a gradual reduction of the entrainment rate during the transition (e.g., Schlemmer & Hohenegger, 2014; Suselj et al., 2019). In the present proposed framework, the deepening happens due to a gradual growth of cloud-updraft interaction, which leads to a gradual reduction of entrainment of dry environmental air in updrafts (Vraciu et al., 2025).

Appendix A: Table of Symbols and Definitions

Table A1 contains definitions of variables and constants found in the text.

Table A1 Variable and Constants Definitions in Alphabetical Order		
Symbol	Default value (units)	Definition
α_0	0.25 (unitless)	constant coefficient (tuning parameter)
α_{gf}	3 (unitless)	constant coefficient (tuning parameter)
B	(m s^{-2})	updraft buoyancy in the bulk plume model
b_j	(m)	integral constant
β_0	(unitless)	constant
β_1	12 (unitless)	constant coefficient (tuning parameter)
β_2	15 (unitless)	constant coefficient (tuning parameter)
c	0.12 (unitless)	constant coefficient (tuning parameter)
c_0	$6 \cdot 10^{-2}$ (unitless)	constant coefficient (tuning parameter)
$CAPE$	(J kg^{-1})	Convective Available Potential Energy
CIN	(J kg^{-1})	Convective Inhibition
Δz_1	(m)	depth of the first cloud layer (see Figure 1)
Δz_2	4,000 (m)	depth of the second cloud layer (see Figure 1)
Δz_3	4,000 (m)	depth of the third cloud layer (see Figure 1)
EL	(m)	equilibrium level

Table A1
Continued

Symbol	Default value (units)	Definition
ϵ	(m^{-1})	fractional entrainment rate in the bulk plume model
g	$9.81 \text{ (m s}^{-2}\text{)}$	gravitational acceleration
γ	(unitless)	parameter (see Equation 10)
κ	$6.75 \cdot 10^{-3} \text{ (m}^{4/3} \text{ W}^{-2/3}\text{)}$	constant coefficient (tuning parameter)
LCL	(m)	lifting condensation level
m_0	(kg m^{-2})	air mass within clouds in the first cloud layer
m_p	(kg m^{-2})	air mass within clouds in the second cloud layer
m_d	(kg m^{-2})	air mass within clouds in the third cloud layer
M_0	($\text{kg m}^{-2} \text{ s}^{-1}$)	mass flux at cloud base (see Figure 1)
M_1	($\text{kg m}^{-2} \text{ s}^{-1}$)	mass flux at the top of shallow cumuli (see Figure 1)
M_2	($\text{kg m}^{-2} \text{ s}^{-1}$)	mass flux at the top of congestus clouds (see Figure 1)
RH	(unitless)	mean troposphere relative humidity
ρ_0	$1.1 \text{ (kg m}^{-3}\text{)}$	air density at cloud base
$\bar{\rho}_0$	$0.944 \text{ (kg m}^{-3}\text{)}$	mean air density in first cloud layer
ρ_1	$0.787 \text{ (kg m}^{-3}\text{)}$	air density at the top of shallow cumuli
$\bar{\rho}_1$	$0.652 \text{ (kg m}^{-3}\text{)}$	mean air density in second cloud layer
ρ_2	$0.516 \text{ (kg m}^{-3}\text{)}$	air density at the top of congestus clouds
$\bar{\rho}_2$	$0.42 \text{ (kg m}^{-3}\text{)}$	mean air density in third cloud layer
ρ_3	$0.324 \text{ (kg m}^{-3}\text{)}$	air density at the top of cumulonimbus clouds
SHF	(W m^{-2})	sensible surface heat flux
σ_0	(unitless)	cloud cover in the first cloud layer (see Figure 1)
σ_1	(unitless)	cloud cover in the second cloud layer (see Figure 1)
σ_2	(unitless)	cloud cover in the third cloud layer (see Figure 1)
σ_{cp}	(unitless)	cold pools fractional area
σ_{gf}	(unitless)	gust fronts fractional area
$\sigma_{int,j}$	(unitless)	interacting updraft fractional area at level $j = \overline{1,2}$
$\sigma_{int,j}^{(0)}$	(unitless)	$\sigma_{int,j}$ in area not affected by cold pools
$\sigma_{int,j}^{(gf)}$	(unitless)	$\sigma_{int,j}$ along gust fronts
σ_u	(unitless)	updraft fractional area immediately below cloud base
$\sigma_{u,0}$	(unitless)	σ_u in the absence of cold pools
$\sigma_u^{(gr)}$	(unitless)	σ_u along gust fronts
$\sigma_u^{(out)}$	(unitless)	σ_u in area not affected by cold pools
t_*	(s)	time required for the deep clouds to reach a fraction of 10^{-5}
τ_0	$25 \cdot 60 \text{ (s)}$	lifetime of clouds in the first cloud layer
$\tau_{0,0}$	$6 \cdot 60 \text{ (s)}$	constant coefficient (tuning parameter) (see Equation 25)
τ_p	$60 \cdot 60 \text{ (s)}$	lifetime of precipitating clouds in the second cloud layer
$\tau_{p,0}$	$9 \cdot 60 \text{ (s)}$	constant coefficient (tuning parameter) (see Equation 25)
τ_d	$3 \cdot 60 \cdot 60 \text{ (s)}$	lifetime of deep clouds in the third cloud layer
$\tau_{d,0}$	$36 \cdot 60 \text{ (s)}$	constant coefficient (tuning parameter) (see Equation 25)
θ_0	300 (K)	reference potential temperature

Table A1
Continued

Symbol	Default value (units)	Definition
w_0	(m s ⁻¹)	mean updraft velocity at cloud base
w_1	(m s ⁻¹)	mean updraft velocity at the top of shallow cumuli
w_2	(m s ⁻¹)	mean updraft velocity at the top of congestus clouds
w_u	(m s ⁻¹)	updraft velocity in the bulk plume model
χ	$2 \cdot 10^{-2}$ (unitless)	constant (see Equation 19)
z_0	(m)	cloud base level (see Figure 1)
z_1	4,000 (m)	level of shallow cumulus top (see Figure 1)
z_2	8,000 (m)	level of congestus clouds top (see Figure 1)
z_3	12,000 (m)	level of cumulonimbus clouds top (see Figure 1)

Conflict of Interest

The authors declare no conflicts of interest relevant to this study.

Data Availability Statement

The LES data presented in Figures 4, 5 and 9 of this work are openly available at Savre (2023a, 2023b). The LES data presented in Figures 6, 7 and 10 are extracted from Kurowski et al. (2018) using an online data digitizer tool (<https://plotdigitizer.com/>), while the LES data presented in Figure 11 are openly available at Haerter (2021). The data obtained with the present dynamical model are obtained by numerically solving the model with the implicit Euler method, as indicated in the text. No new experimental, observational, or LES data have been generated for this work.

Acknowledgments

The author thanks two anonymous reviewers and Robert Plant for valuable comments and feedback on the manuscript. The author is financially supported at the University of Reading by the European Union under the Marie Skłodowska-Curie Actions (MSCA) Postdoctoral Fellowships—European Fellowships, Project UPDRAFT (101201579). Views and opinions expressed are those of the author only and do not necessarily reflect those of the European Union or the European Research Executive Agency (REA). Neither the European Union nor the granting authority can be held responsible for them.

References

- Arakawa, A., & Schubert, W. H. (1974). Interaction of a cumulus cloud ensemble with the large-scale environment, part I. *Journal of the Atmospheric Sciences*, 31(3), 674–701. [https://doi.org/10.1175/1520-0469\(1974\)031<0674:IOACCE>2.0.CO;2](https://doi.org/10.1175/1520-0469(1974)031<0674:IOACCE>2.0.CO;2)
- Bechtold, P., Chaboureaud, J.-P., Beljaars, A., Betts, A., Köhler, M., Miller, M., & Redelsperger, J.-L. (2004). The simulation of the diurnal cycle of convective precipitation over land in a global model. *Quarterly Journal of the Royal Meteorological Society*, 130(604), 3119–3137. <https://doi.org/10.1256/qj.03.103>
- Bechtold, P., Semane, N., Lopez, P., Chaboureaud, J.-P., Beljaars, A., & Bormann, N. (2014). Representing equilibrium and nonequilibrium convection in large-scale models. *Journal of the Atmospheric Sciences*, 71(2), 734–753. <https://doi.org/10.1175/JAS-D-13-0163.1>
- Böing, S. J., Jonker, H. J. J., Siebesma, A. P., & Grabowski, W. W. (2012). Influence of the subcloud layer on the development of a deep convective ensemble. *Journal of the Atmospheric Sciences*, 69(9), 2682–2698. <https://doi.org/10.1175/JAS-D-11-0317.1>
- Chakraborty, S., Schiro, K. A., Fu, R., & Neelin, J. D. (2018). On the role of aerosols, humidity, and vertical wind shear in the transition of shallow-to-deep convection at the green ocean Amazon 2014/5 site. *Atmospheric Chemistry and Physics*, 18(15), 11135–11148. <https://doi.org/10.5194/acp-18-11135-2018>
- Chen, J., Hagos, S., Fast, J., & Feng, Z. (2025). Predicting the evolution of shallow cumulus clouds with a Lotka-Volterra like model. *Journal of Advances in Modeling Earth Systems*, 17(2), e2023MS003739. <https://doi.org/10.1029/2023MS003739>
- Colin, M., Sherwood, S., Geoffroy, O., Bony, S., & Fuchs, D. (2019). Identifying the sources of convective memory in cloud-resolving simulations. *Journal of the Atmospheric Sciences*, 76(3), 947–962. <https://doi.org/10.1175/JAS-D-18-0036.1>
- Colin, M., & Sherwood, S. C. (2021). Atmospheric convection as an unstable predator-prey process with memory. *Journal of the Atmospheric Sciences*, 78(11), 3781–3797. <https://doi.org/10.1175/JAS-D-20-0337.1>
- Couvreux, F., Roehrig, R., Rio, C., Lefebvre, M.-P., Komori, T., Derbyshire, S., et al. (2015). Representation of daytime moist convection over the semi-arid tropics by parametrizations used in climate and meteorological models. *Quarterly Journal of the Royal Meteorological Society*, 141(691), 2220–2236. <https://doi.org/10.1002/qj.2517>
- Cui, Z., Zhang, G. J., Wang, Y., & Xie, S. (2021). Understanding the roles of convective trigger functions in the diurnal cycle of precipitation in the NCAR CAM5. *Journal of Climate*, 34(15), 6473–6489. <https://doi.org/10.1175/JCLI-D-20-0699.1>
- Daleu, C. L., Plant, R., Woolnough, S., Stirling, A., & Harvey, N. (2020). Memory properties in cloud-resolving simulations of the diurnal cycle of deep convection. *Journal of Advances in Modeling Earth Systems*, 12(8), e2019MS001897. <https://doi.org/10.1029/2019MS001897>
- De Rooy, W. C., Bechtold, P., Fröhlich, K., Hohenegger, C., Jonker, H., Mironov, D., et al. (2013). Entrainment and detrainment in cumulus convection: An overview. *Quarterly Journal of the Royal Meteorological Society*, 139(670), 1–19. <https://doi.org/10.1002/qj.1959>
- Efstathiou, G. A., Plant, R. S., & Chow, F. K. (2024). Grey-zone simulations of shallow-to-deep convection transition using dynamic subgrid-scale turbulence models. *Quarterly Journal of the Royal Meteorological Society*, 150(764), 4306–4328. <https://doi.org/10.1002/qj.4817>
- Eytan, E., Arieli, Y., Khain, A., Altartaz, O., Pinsky, M., Gavze, E., & Koren, I. (2024). The role of the toroidal vortex in cumulus clouds' entrainment and mixing. *Journal of Geophysical Research: Atmospheres*, 129(14), e2023JD039493. <https://doi.org/10.1029/2023JD039493>

- Feingold, G., Koren, I., Yamaguchi, T., & Kazil, J. (2015). On the reversibility of transitions between closed and open cellular convection. *Atmospheric Chemistry and Physics*, *15*(13), 7351–7367. <https://doi.org/10.5194/acp-15-7351-2015>
- Fiévet, R., Meyer, B., & Haerter, J. O. (2023). On the sensitivity of convective cold pools to mesh resolution. *Journal of Advances in Modeling Earth Systems*, *15*(8), e2022MS003382. <https://doi.org/10.1029/2022MS003382>
- Fu, H., & O'Neill, M. E. (2025). Mean cold pool size of quasi-equilibrium convection. Part I: Why do cold pools collide? *Journal of the Atmospheric Sciences*, *82*(2), 237–250. <https://doi.org/10.1175/JAS-D-23-0143.1>
- Fuglestedt, H. F., & Haerter, J. O. (2020). Cold pools as conveyor belts of moisture. *Geophysical Research Letters*, *47*(12), e2020GL087319. <https://doi.org/10.1029/2020GL087319>
- Grabowski, W. (2023). Daytime convective development over land: The role of surface forcing. *Quarterly Journal of the Royal Meteorological Society*, *149*(756), 2800–2819. <https://doi.org/10.1002/qj.4532>
- Grabowski, W., Bechtold, P., Cheng, A., Forbes, R., Halliwell, C., Khairoutdinov, M., et al. (2006). Daytime convective development over land: A model intercomparison based on LBA observations. *Quarterly Journal of the Royal Meteorological Society*, *132*(615), 317–344. <https://doi.org/10.1256/qj.04.147>
- Guichard, F., Petch, J., Redelsperger, J.-L., Bechtold, P., Chaboureaud, J.-P., Cheinet, S., et al. (2004). Modelling the diurnal cycle of deep precipitating convection over land with cloud-resolving models and single-column models. *Quarterly Journal of the Royal Meteorological Society*, *130*(604), 3139–3172. <https://doi.org/10.1256/qj.03.145>
- Haerter, J. O. (2021). 1D (time) and 2D (time and vertical coordinate) data for the cases DIU-500m, RCE-500m and DIU2RCE-500m [Dataset]. *Zenodo*. <https://doi.org/10.5281/zenodo.4898182>
- Harvey, N. J., Daleu, C. L., Stratton, R. A., Plant, R. S., Woolnough, S. J., & Stirling, A. J. (2022). The impact of surface heterogeneity on the diurnal cycle of deep convection. *Quarterly Journal of the Royal Meteorological Society*, *148*(749), 3509–3527. <https://doi.org/10.1002/qj.4371>
- Hernández Pardo, L., Morrison, H., & Possner, A. (2025). Dynamics of downdrafts around a growing convective cloud: A numerical study. *Journal of Geophysical Research: Atmospheres*, *130*(22), e2025JD044236. <https://doi.org/10.1029/2025JD044236>
- Hohenegger, C., & Bretherton, C. S. (2011). Simulating deep convection with a shallow convection scheme. *Atmospheric Chemistry and Physics*, *11*(20), 10389–10406. <https://doi.org/10.5194/acp-11-10389-2011>
- Jensen, G. G., Fiévet, R., & Haerter, J. O. (2022). The diurnal path to persistent convective self-aggregation. *Journal of Advances in Modeling Earth Systems*, *14*(5), e2021MS002923. <https://doi.org/10.1029/2021MS002923>
- Jo, E., Feng, Z., Varble, A. C., Marquis, J. N., & Gustafson, W. I., Jr. (2025). The effect of updraft entrainment on convective cell deepening in realistic large-eddy simulations. *Journal of the Atmospheric Sciences*, *82*(7), 1361–1379. <https://doi.org/10.1175/JAS-D-24-0218.1>
- Khairoutdinov, M., & Randall, D. (2006). High-resolution simulation of shallow-to-deep convection transition over land. *Journal of the Atmospheric Sciences*, *63*(12), 3421–3436. <https://doi.org/10.1175/JAS3810.1>
- Koren, I., & Feingold, G. (2011). Aerosol–cloud–precipitation system as a predator–prey problem. *Proceedings of the National Academy of Sciences of the United States of America*, *108*(30), 12227–12232. <https://doi.org/10.1073/pnas.1101777108>
- Kurowski, M. J., Paris, A., & Teixeira, J. (2024). The unique behavior of vertical velocity in developing deep convection. *Geophysical Research Letters*, *51*(20), e2024GL110425. <https://doi.org/10.1029/2024GL110425>
- Kurowski, M. J., Suselj, K., Grabowski, W. W., & Teixeira, J. (2018). Shallow-to-deep transition of continental moist convection: Cold pools, surface fluxes, and mesoscale organization. *Journal of the Atmospheric Sciences*, *75*(12), 4071–4090. <https://doi.org/10.1175/JAS-D-18-0031.1>
- Manco, J. A., & Figueroa, S. N. (2025). Large eddy simulation of the diurnal cycle of shallow convection in the central amazon. *Atmosphere*, *16*(7), 789. <https://doi.org/10.3390/atmos16070789>
- Miller, G. A., Stier, P., & Christensen, H. M. (2025). Characterizing uncertainty in deep convection triggering using explainable machine learning. *Journal of the Atmospheric Sciences*, *82*(6), 1093–1111. <https://doi.org/10.1175/JAS-D-24-0085.1>
- Morrison, H. (2017). An analytic description of the structure and evolution of growing deep cumulus updrafts. *Journal of the Atmospheric Sciences*, *74*(3), 809–834. <https://doi.org/10.1175/JAS-D-16-0234.1>
- Morrison, H., Peters, J. M., Chandrakar, K. K., & Sherwood, S. C. (2022). Influences of environmental relative humidity and horizontal scale of subcloud ascent on deep convective initiation. *Journal of the Atmospheric Sciences*, *79*(2), 337–359. <https://doi.org/10.1175/JAS-D-21-0056.1>
- Nober, F. J., & Graf, H.-F. (2005). A new convective cloud field model based on principles of self-organisation. *Atmospheric Chemistry and Physics*, *5*(10), 2749–2759. <https://doi.org/10.5194/acp-5-2749-2005>
- Pan, D.-M., & Randall, D. D. (1998). A cumulus parameterization with a prognostic closure. *Quarterly Journal of the Royal Meteorological Society*, *124*(547), 949–981. <https://doi.org/10.1002/qj.49712454714>
- Peters, J. M., Chavas, D. R., Su, C.-Y., Morrison, H., & Coffey, B. E. (2023). An analytic formula for entraining CAPE in midlatitude storm environments. *Journal of the Atmospheric Sciences*, *80*(9), 2165–2186. <https://doi.org/10.1175/JAS-D-23-0003.1>
- Pinsky, M., Eytan, E., Gavze, E., & Khain, A. (2023). Vortex structure of head bubble in convective cloud starting plume. *Journal of the Atmospheric Sciences*, *80*(8), 2091–2113. <https://doi.org/10.1175/JAS-D-22-0122.1>
- Plant, R., & Yano, J.-I. (2011). Comments on “An ensemble cumulus convection parameterization with explicit cloud treatment”. *Journal of the Atmospheric Sciences*, *68*(7), 1541–1544. <https://doi.org/10.1175/2011JAS3728.1>
- Rio, C., Grandpeix, J.-Y., Hourdin, F., Guichard, F., Couvreux, F., Lafore, J.-P., et al. (2013). Control of deep convection by sub-cloud lifting processes: The ALP closure in the LMDZ5B general circulation model. *Climate Dynamics*, *40*(9–10), 2271–2292. <https://doi.org/10.1007/s00382-012-1506-x>
- Rio, C., Hourdin, F., Grandpeix, J.-Y., & Lafore, J.-P. (2009). Shifting the diurnal cycle of parameterized deep convection over land. *Geophysical Research Letters*, *36*(7). <https://doi.org/10.1029/2008GL036779>
- Romps, D. M. (2010). A direct measure of entrainment. *Journal of the Atmospheric Sciences*, *67*(6), 1908–1927. <https://doi.org/10.1175/2010JAS3371.1>
- Savre, J. (2023a). Outputs from new LBA simulations. Part I: Baseline case [Dataset]. *Zenodo*. <https://doi.org/10.5281/zenodo.10409139>
- Savre, J. (2023b). Outputs from new LBA simulations. Part III: Suppressed cold pools [Dataset]. *Zenodo*. <https://doi.org/10.5281/zenodo.10417550>
- Savre, J., & Craig, G. (2023). Fitting cumulus cloud size distributions from idealized cloud resolving model simulations. *Journal of Advances in Modeling Earth Systems*, *15*(5), e2022MS003360. <https://doi.org/10.1029/2022MS003360>
- Savre, J., Ekman, A. M. L., & Svensson, G. (2014). Technical note: Introduction to MIMICA, a large-eddy simulation solver for cloudy planetary boundary layers. *Journal of Advances in Modeling Earth Systems*, *6*(3), 630–649. <https://doi.org/10.1002/2013MS000292>
- Schlemmer, L., & Hohenegger, C. (2014). The formation of wider and deeper clouds as a result of cold-pool dynamics. *Journal of the Atmospheric Sciences*, *71*(8), 2842–2858. <https://doi.org/10.1175/JAS-D-13-0170.1>

- Sherwood, S. C., Hernández-Deckers, D., Colin, M., & Robinson, F. (2013). Slippery thermals and the cumulus entrainment paradox. *Journal of the Atmospheric Sciences*, *70*(8), 2426–2442. <https://doi.org/10.1175/JAS-D-12-0220.1>
- Song, J., Song, F., Feng, Z., Leung, L. R., Li, C., & Wu, L. (2024). Realistic precipitation diurnal cycle in global convection-permitting models by resolving mesoscale convective systems. *Geophysical Research Letters*, *51*(13), e2024GL109945. <https://doi.org/10.1029/2024GL109945>
- Suselj, K., Kurowski, M. J., & Teixeira, J. (2019). A unified eddy-diffusivity/mass-flux approach for modeling atmospheric convection. *Journal of the Atmospheric Sciences*, *76*(8), 2505–2537. <https://doi.org/10.1175/JAS-D-18-0239.1>
- Tao, C., Xie, S., Ma, H.-Y., Bechtold, P., Cui, Z., Vaillancourt, P. A., et al. (2023). Diurnal cycle of precipitation over the tropics and central United States: Intercomparison of general circulation models. *Quarterly Journal of the Royal Meteorological Society*, *150*(759), 911–936. <https://doi.org/10.1002/qj.4629>
- Tian, Y., & Zhang, Y. (2025). Factors controlling precipitation onset and maintenance: Inferences from large eddy simulations of two afternoon deep convective regimes over Amazon. *Geophysical Research Letters*, *52*(12), e2024GL113920. <https://doi.org/10.1029/2024GL113920>
- Tian, Y., Zhang, Y., Klein, S. A., & Schumacher, C. (2021). Interpreting the diurnal cycle of clouds and precipitation in the ARM GoAmazon observations: Shallow to deep convection transition. *Journal of Geophysical Research: Atmospheres*, *126*(5), e2020JD033766. <https://doi.org/10.1029/2020JD033766>
- Tompkins, A. M. (2001). Organization of tropical convection in low vertical wind shears: The role of cold pools. *Journal of the Atmospheric Sciences*, *58*(13), 1650–1672. [https://doi.org/10.1175/1520-0469\(2001\)058<1650:OOTCL>2.0.CO;2](https://doi.org/10.1175/1520-0469(2001)058<1650:OOTCL>2.0.CO;2)
- Torri, G., Kuang, Z., & Tian, Y. (2015). Mechanisms for convection triggering by cold pools. *Geophysical Research Letters*, *42*(6), 1943–1950. <https://doi.org/10.1002/2015GL063227>
- Varble, A. C., Feng, Z., Marquis, J. N., Zhang, Z., Geiss, A., Hardin, J. C., & Jo, E. (2024). Updraft width modulates ambient atmospheric controls on convective cloud depth. *Journal of Geophysical Research: Atmospheres*, *129*(23), e2024JD041769. <https://doi.org/10.1029/2024JD041769>
- Viscardi, L. A. M., Torri, G., Adams, D. K., & Barbosa, H. d. M. J. (2025). Sensitivity of the shallow-to-deep convective transition to moisture and wind shear in the amazon. *Journal of Advances in Modeling Earth Systems*, *17*(4), e2024MS004238. <https://doi.org/10.1029/2024MS004238>
- Vraciu, C. V. (2022). On the energy-consistent plume model in the convective boundary layer. *Dynamics of Atmospheres and Oceans*, *100*, 101330. <https://doi.org/10.1016/j.dynatmoce.2022.101330>
- Vraciu, C. V. (2024). Generalized eddy-diffusivity mass-flux formulation for the parametrization of atmospheric convection and turbulence. *Quarterly Journal of the Royal Meteorological Society*, *150*(761), 2316–2337. <https://doi.org/10.1002/qj.4711>
- Vraciu, C. V., Kruse, I. L., & Haerter, J. O. (2023). The role of passive cloud volumes in the transition from shallow to deep atmospheric convection. *Geophysical Research Letters*, *50*(23), e2023GL105996. <https://doi.org/10.1029/2023GL105996>
- Vraciu, C. V., Savre, J., & Colin, M. (2025). The rapid transition from shallow to precipitating convection as a predator-prey process. *Journal of Advances in Modeling Earth Systems*, *17*(2), e2024MS004630. <https://doi.org/10.1029/2024MS004630>
- Wagner, T. M., & Graf, H.-F. (2010). An ensemble cumulus convection parameterization with explicit cloud treatment. *Journal of the Atmospheric Sciences*, *67*(12), 3854–3869. <https://doi.org/10.1175/2010JAS3485.1>
- Wu, C.-M., Stevens, B., & Arakawa, A. (2009). What controls the transition from shallow to deep convection? *Journal of the Atmospheric Sciences*, *66*(6), 1793–1806. <https://doi.org/10.1175/2008JAS2945.1>
- Xie, S., Wang, Y.-C., Lin, W., Ma, H.-Y., Tang, Q., Tang, S., et al. (2019). Improved diurnal cycle of precipitation in E3SM with a revised convective triggering function. *Journal of Advances in Modeling Earth Systems*, *11*(7), 2290–2310. <https://doi.org/10.1029/2019MS001702>
- Xu, X., Sun, C., Lu, C., Liu, Y., Zhang, G. J., & Chen, Q. (2021). Factors affecting entrainment rate in deep convective clouds and parameterizations. *Journal of Geophysical Research: Atmospheres*, *126*(15), e2021JD034881. <https://doi.org/10.1029/2021JD034881>
- Yano, J.-I., & Plant, R. (2012a). Finite departure from convective quasi-equilibrium: Periodic cycle and discharge–recharge mechanism. *Quarterly Journal of the Royal Meteorological Society*, *138*(664), 626–637. <https://doi.org/10.1002/qj.957>
- Yano, J.-I., & Plant, R. S. (2012b). Interactions between shallow and deep convection under a finite departure from convective quasi equilibrium. *Journal of the Atmospheric Sciences*, *69*(12), 3463–3470. <https://doi.org/10.1175/JAS-D-12-0108.1>
- Zhuang, Y., Fu, R., Marengo, J. A., & Wang, H. (2017). Seasonal variation of shallow-to-deep convection transition and its link to the environmental conditions over the Central Amazon. *Journal of Geophysical Research: Atmospheres*, *122*(5), 2649–2666. <https://doi.org/10.1002/2016JD025993>